

Contents lists available at ScienceDirect

Tectonophysics

journal homepage: www.elsevier.com/locate/tecto





A new generation Griggs apparatus with active acoustic monitoring

Arefeh Moarefvand ^{a,*}, Julien Gasc ^a, Julien Fauconnier ^a, Marie Baïsset ^b, Eric Burdette ^c, Loïc Labrousse ^b, Alexandre Schubnel ^a

- ^a Laboratoire de Géologie, École Normale Supérieure/CNRS UMR 8538, PSL University, Paris, France
- ^b ISTEP, Sorbonne Université, Paris, France
- ^c Department of Earth, Environmental and Planetary Sciences, Brown University, Providence, RI, USA

ARTICLE INFO

Keywords: Active acoustic monitoring P-wave velocities Griggs apparatus Metamorphic reactions High-pressure experiment $\alpha \to \beta$ quartz transition

ABSTRACT

High pressure and temperature experiments are necessary to understand geological processes at deep earth conditions. Here, we present a new generation *Griggs*-type apparatus, designed to perform deformation experiments at P-T conditions of the lower crust and upper mantle, i.e. up to 5 GPa and 1000 °C. We first detail the experimental design, set-up and procedure, as well as the calibration protocol of the apparatus. The main innovation of this new set-up is the development of an active acoustic monitoring pulse-transmission technique, which enables us to monitor the evolution of P-wave elastic velocities, at 5 MHz, contemporaneously with deformation. This may provide information on the evolution of the microstructure, in particular when mineralogical (metamorphic) reactions are taking place. For instance, P-wave velocity variations across the $\alpha \to \beta$ quartz transition are recorded for the first time within a *Griggs* apparatus, at 0.5 and 0.8 GPa. This new set-up opens up important perspectives for the study of the complex couplings that may take place between mineral reactions and deformation under in lithospheric stress and temperature conditions.

1. Introduction

The study of rock deformation under Earth's pressure and temperature conditions is a relatively young field of science that emerged with the advent of the first tri-axial apparatus designed by Theodore von Kármán in 1910, which could deform rock samples up to lateral confinement stresses of up to 165 MPa confinement, i.e. the pressure prevalent at 5 km depth (Vásárhelyi, 2010). Shortly afterwards, using a new sealing technology (famously now referred to as the Bridgman seal), Percy Bridgman reached the symbolic frontier of the gigapascal in a pressure device (Bridgman, 1914; Bridgman, 1912), i.e. the pressure at approximately 30 km depth.

In 1936, David T. Griggs reported "a series of experiments to investigate the physical processes underlying rock deformation. The apparatus used took advantage of recent developments in highpressure technique by Bridgman (...). The relation between strength and confining pressure was investigated up to 11000 atmospheres" (i.e. 1.1 GPa). These pioneering experiments were the foundation to his seminal "Theory of Mountain building" (1939), where he argued, on the basis of experimental data, that thermal convection currents in the Earth's mantle might be responsible for the distribution of mountain-building episodes in the Earth's crust. After WWII,

Griggs and his PhD. students at UCLA laid foundations of the emerging field of high-pressure and temperature rock deformation, with the development of several apparatuses that either became standards or inspired further experimental developments (Getting and Christie, 1994).

Amongst these, the modified solid-medium piston cylinder apparatus still colloquially bears the name of the Griggs-apparatus. It is a device with cylindrical geometry, modified in the sense that an extra-piston enables the users to deform centimeter-size rock samples at conditions of the Earth's lithosphere. The Griggs-apparatus was first designed in the 1960s and has been modified and improved several times over the years, most notably by (Tullis and Tullis, 1986) who extended its pressure range to 5 GPa. The cell assembly has also been drastically improved (Green and Borch, 1989; Mirwald et al., 1975). The stress and strain resolutions of the apparatus have been extensively discussed and compared for different cell (Holyoke and Kronenberg, 2010; Kido et al., 2016). This device, along with the Paterson gas-medium apparatus (Paterson, 1970) whose pressure range is limited to 500 MPa, have provided much of the information available on the plastic deformation mechanisms and flow laws of minerals and rocks (Karato et al., 2002; Paterson and Wong, 2005; Tullis, 1979).

E-mail address: moaref@geologie.ens.fr (A. Moarefvand).

^{*} Corresponding author.

With the advent of the Deformation-DIA apparatus (Wang et al., 2003), the field of experimental rock deformation has now been extended to conditions reaching that of the lower mantle (above 20 GPa). Mounted on a synchrotron, the D-DIA enables in-situ access to deformation mechanisms, direct monitoring of crystalline texture development and/or evolving mineralogy under high stress, pressure and temperature (Incel et al., 2017). The primary drawbacks of this apparatus and the need for a small, intense beam of synchrotron light is that measurements of strain and stress are restricted to small (millimetric) samples, and limitations of beamtime to perform long-term or large sets of experiments.

In the 1960s, Albert Francis Birch, developed a device to monitor ultrasonic waves velocities through rocks under hydrostatic conditions up to 1GPa at room temperature, laying the foundation to the empirical *Birch's law*, which states that elastic wave velocities increase linearly with bulk density (Birch, 1961; Birch, 1960). The experimental technique used by Birch was based on the piezoelectric effect: high amplitude - high frequency voltage is sent to a polarized piezo-ceramic source transducer, which converts this voltage into motion. The elastic waves generated by this motion then travel through a specimen and are recovered by a piezo-ceramic receiver, which converts motion back into a low amplitude high frequency voltage. The time of flight between the source and the receiver is measured and permits the calculation of elastic wave velocities in the specimen.

This simple in situ non-destructive monitoring technique has been modified and adapted to various high-pressure and temperature devices in order to measure wave-speeds of crustal rocks at crustal pressure and temperature conditions, as applied by (Christensen, 1979) or (Kern and Richter, 1981), to measure compressive and shear wave velocities Vp and Vs, respectively, in rock specimens up to 600 MPa and 700 °C. A modified technique, known as the pulse-echo interferometry method, where the same transducer is used as both source and receiver, was later adapted to the multi-anvil apparatus by (Li et al., 1996), and enabled measurements of elastic wave velocities at mantle transition zone pressure and temperature conditions (Gwanmesia et al., 1990). The technique has also recently been adapted to the Diamond Anvil Cell (DAC) by (Jacobsen et al., 2002). In both cases, elastic wave velocities are best retrieved under synchrotron light, in order to measure variations in sample's length (Li and Liebermann, 2007).

Here, we report on a third generation *Griggs* apparatus, recently installed at the Laboratoire de Géologie of the Ecole Normale Supérieure de Paris. This apparatus, fully servo-controlled with hydraulics, has a similar pressure and temperature range as that of the second generation, up to 5 GPa and 1200 °C (Précigout et al., 2018). However, its main innovation resides in its capability of performing active ultrasonic monitoring contemporaneously with rock deformation at high pressure and temperature conditions. After a short description of the apparatus design and of the experimental methods, we show a few examples where elastic wave velocities were monitored during deformation at high pressure and temperature, and how their variations may be a good nondestructive proxy to track phase transitions and mineral reactions.

2. Experimental set-up

This section consists of the first description of the *Griggs* apparatus recently installed in *École Normale Supérieure de Paris*. The current sample's assembly, the mechanical set-up, including hydraulics, heating and cooling systems, and the acoustic monitoring set-up are detailed in the following.

2.1. Sample's assembly

At the core of our apparatus is a 20 mm diameter solid-medium sample assembly (Fig. 1). The sample itself (\sim 4.5 mm in diameter, and 10 mm height), located at the center of this assembly, consists either of a sample core-drilled from natural or synthetic rocks, or of a fine-

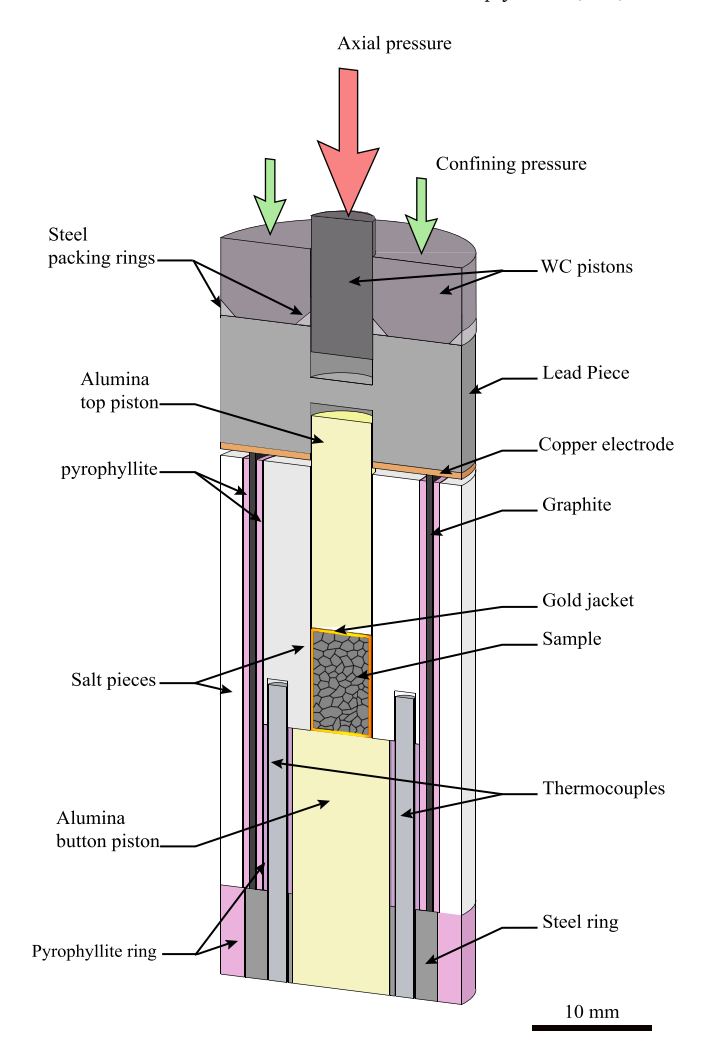


Fig. 1. Vertical cross-section of the sample's assembly.

grained powder of known grain size and mineralogy. The sample is encapsulated within a gold (or platinum) jacket of $0.25~\mathrm{mm}$ wall-thickness.

The confining pressure medium around the sample consists of highly-compacted fine-grained NaCl powder (99.9% purity). Thanks to its low viscosity, NaCl transmits a quasi-hydrostatic (uniform) confining pressure to the sample. Two holes are drilled to half sample-height within the internal salt piece to place thermocouples and monitor the temperature inside the assembly. In general, sheathed K-type (Ni-chromium/Ni-Alumel) thermocouples (Omega XL-K-M, 1.5 mm diam) are used because of their wide range of temperature, from room temperature to approximately 1100 °C. They are inserted within the assembly after soldering, through the bottom hard-fired pyrophyllite and hardened steel parts.

Joule heating is performed via a graphite furnace sleeve (0.5 mm wall thickness), mechanically reinforced by inner and outer hard-fired pyrophyllite sleeves. AC-current flows into the furnace via the hard-ened steel piece on which it rests. That steel piece is directly connected to an electrically insulated 'bottom-plate', made of tungsten carbide (WC), which acts as one of the electrodes. Current flows out of the furnace via a copper disc placed on top of the assembly that connects to the pressure vessel, which acts as a zero potential (ground) electrode.

Axial load is applied via a 5 mm diameter piston at the top of the sample, which in turn, sits on an 8 mm diameter pedestal (Fig. 1). Both the piston and the pedestal are made of non-porous alumina (Al_2O_3), a material known to retain high strength even at high temperature. Therefore, both the alumina piston and pedestal deform elastically

during the deformation stage of our experiments. A disk of lead separates the top WC pistons from the assembly, with the aim of keeping the sample in hydrostatic condition during pressurization. Lead, because of the low strength in the outermost, colder portions of the assembly, acts as a pressure/load buffer. Finally, two mitre rings (Fig. 1), made of high-grade steel, prevent the lead and the salt from flowing out of the assembly upon pressurization/deformation.

2.2. Mechanical Set up

The apparatus consists of a pressure vessel and two hydraulic rams, framed by three horizontal platens and four vertical columns (Fig. 2). Strecon, a Danish company, manufactured all of our vessels. The pressure vessel (Figs. 2 & 3) has an outer diameter of 300 mm, a thickness of 55 mm, and includes three parts. First, a cylindrical core that consists of a 100 mm outer diameter WC die (with high Co-binding), with a 20 mm cylindrical inner borehole, where the sample assembly is inserted during the experiment. Second, a strip-steel container is made of high-strength steel that remains fully elastic up to approximately 2GPa. The core was forced mechanically into the container, in order to obtain optimal radial pre-stressing of the WC die. The interference angle between the core and the container was of 0.4°. That way, the ultimate strength of core is approximately 5 GPa, i.e. twice the initial compressive strength of WC. Finally, the pressure vessel is sandwiched between two cooling plates, in

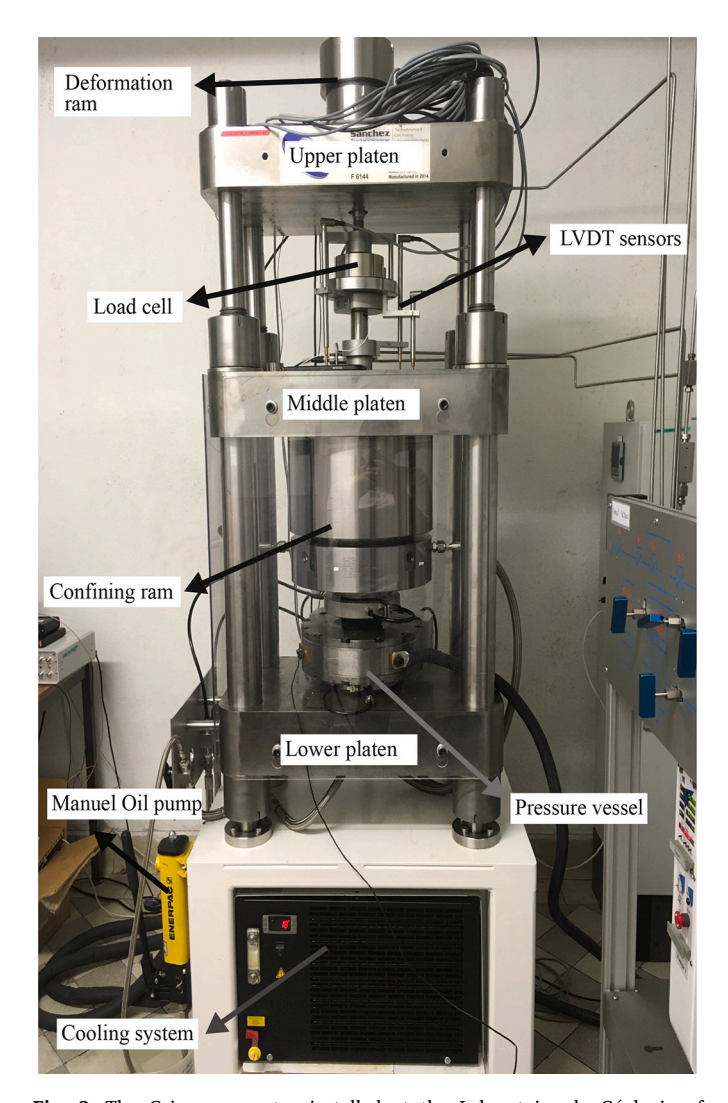


Fig. 2. The Griggs apparatus installed at the Laboratoire de Géologie of ENS Paris.

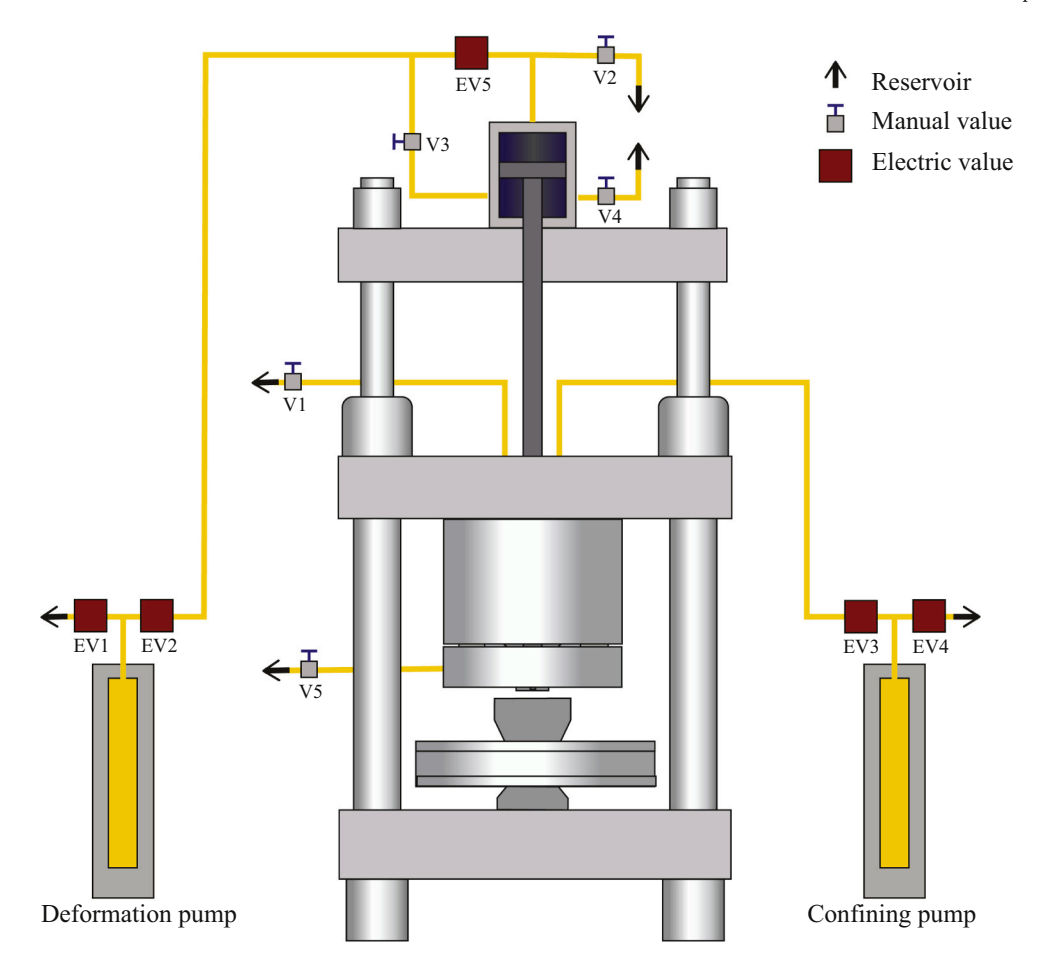
which water-based coolant is continuously flowed so that the outer temperature of the vessel remains below 40 °C during the experiments.

The main hydraulic ram (Fig. 2) is attached to the middle platen. It consists of a double piston (Fig. 3), which can develop a total force of 3.6 MN (i.e., 360 tons). The outer piston, referred to as the end-load piston, loads the WC core in order to avoid disking and splitting of the core during the experiments. The end-load is transmitted to the WC core via a hardened steel spacer. The inner part of the piston, referred to as confining pressure (or σ_3) piston, transmits the load, to a cylindrical WC piston of 20 mm diameter and onto the cell assembly via a WC piston. The ram is designed in such a way that the ratio between the load transmitted to the WC core and that transmitted to the assembly is fixed and equal 1.5. This way 60% of the load applied by the ram is transmitted to the core, while the remaining 40% is transmitted to the assembly. The maximum load (3.6 MN) corresponds to a confining pressure of 4.85 GPa inside the sample assembly. The displacement of the ram can be as large as 50 mm, monitored via a LVDT (Linear Variable Differential Transformer) placed between the upper and middle platens. The ram is servocontrolled, either by pressure or displacement (constant pressure, oil influx or outflux inside the upper or lower pressure chambers), via a 150 MPa high-pressure syringe pump of 100 mL capacity (Fig. 3).

The deformation ram (Figs. 2 & 3) is attached to the upper platen. The applied load produced by this ram is transmitted to the sample through the main hydraulic ram (Fig. 2), via a deformation column made of a hardened steel piston, a WC spacer, a WC piston, and a 50 mm long - 5 mm diameter WC piston. The latter sits within the lead piece placed atop the sample assembly. Note that the hardened steel piston has a 2 mm center hole, in order to instrument the WC spacer with an acoustic transducer (see Fig. 3 and Section 2.3). At maximum load (235kN), the theoretical axial stress (σ 1) applied to a 5 mm diameter sample reaches 12 GPa. An industrial load cell (HBM 1-C2/200KN) monitors the load developed by the deformation ram with an accuracy of 0.1kN (i.e. \pm / 5 MPa on a 5 mm diameter sample). Two LVDTs, one long range (0–50 mm) and one short range (0–10 mm), monitor the displacement of the deformation ram (maximum course 50 mm). The accuracy of the short range LVDT (HBM 1-WA/10MM-T) is better than $0.1 \mu m$; this latter LVDT is therefore used during the deformation stage of the experiment to determine the assembly column shortening from which sample shortening is deduced after correcting for elastic distortion of the load system. The deformation ram is servo-controlled, either by pressure or by displacement (constant pressure, oil influx or outflux inside the upper or lower pressure chambers), via a 30 MPa highpressure syringe pump of 1000 mL capacity (Fig. 3).

The pressures inside the upper pressure chamber of both rams and inside the syringe pumps are monitored using high-resolution pressure transducers with a resolution of 1 kPa. Both syringe pumps are softwarecontrolled and can be controlled linearly, either in pressure or flow rate. In pressure mode, a target (increase or decrease) pressure can be set along with a ramp. In flow mode, a target volume of injection can be set, along with a flow rate. Constant displacement rate of the ram can be achieved using the pump in constant flow rate mode. Constant pressure (or stress) can be achieved using the pump in controlled pressure mode. The minimum oil flow rate of 0.01 ml/h within the deformation ram corresponds, to a displacement of approximately 0.5 µm/h, i.e. a minimum strain rate of approximately 2×10^{-8} /s for a 10 mm long sample. The minimum pressurization rate of 1 kPa/s within the main ram corresponds to a pressurization rate of the sample assembly of approximately 0.1 GPa/h. A mix of air-actuated and manual high-pressure valves drives the direction of oil flow in or out from the pumps (and rams) and changes configuration during loading and unloading. Schematics of the hydraulics are detailed in Fig. 3.

Hydraulic rams, the frame and the syringe pumps were manufactured, custom made, by Sanchez technologies - Corelab France. Data coming from the 3 LVDTs, the load cell, the two pressure transducers and the two thermocouples are digitized using a QuantumX (HBM) data



 $\textbf{Fig. 3.} \ \ \textbf{Schematics of the hydraulic system.}$

recorder and pre-processed using the software CatmanEasy (HBM). The maximum data sampling rate is 2 kHz, but typical experiments are recorded at $1-10~\rm{Hz}$.

2.3. Heating and cooling units

The resistive graphite furnace heats the assembly at low voltage (max 15 V) and high current (max 400 A), provided by a 24 V-2.5A power supply (Omron S8VK-G06024), a phase-angle thyristor power controller (Jumo GmbH TYA 201), a 6 kW (15 V/400A) transformer (SBA Trafotech GmbH, USI 128–6000) and a Eurotherm controller (3504), all enclosed within an electric cabinet manufactured by Max-Voggenreiter GmbH. Typically, we observe a linear relationship between input power and the temperature read by the thermocouples within the sample assembly, up to $\approx 1100\,^{\circ}\text{C}$, a temperature reached for a typical power of approximately 2.5 kW and a furnace resistance of 20 m Ω .

The Eurotherm heat controller software can be used either in power control mode (PC) or in temperature control mode (TC). Temperature or power set points can also be given manually. For safety purposes, the system will quench automatically if both thermocouples fail when in TC mode.

In order to cool the vessel, a 4 kW-cooling unit constantly flows chilled water within a closed-loop, through the cooling plates placed above and below the pressure vessel, around the bottom-plate and the end-load piston spacer. The cooling system regulates the cooling water temperature above the dew-point in the room, typically at 15 $^{\circ}$ C. A PT-100 probe fixed on the outside wall of the pressure vessel monitors its temperature. With this efficient cooling, the vessel's outside wall

typically reaches a temperature of 30 $^{\circ}\text{C},$ when thermocouples read a temperature above 1000 $^{\circ}\text{C}$ inside the assembly. For safety purpose, the heating system is programmed to quench automatically, and both rams will also stop, as soon as the vessel's outer wall temperature goes beyond 40 $^{\circ}\text{C}.$

2.4. Acoustic set-up

Our equipment was designed specifically to perform active acoustic monitoring during rock deformation experiments at high pressure and temperature. Fig. 4 displays the schematics of our ultrasound recording system.

Two industrial ultrasonic transducers are used, both sensitive to longitudinal (P) waves, i.e. elastic waves propagating and vibrating along the direction of maximum compression (σ_1). The bottom transducer (Olympus V110, 5 MHz center frequency) is glued on a 0.25 mm thick alumina ceramic disk with a high temperature 2 components epoxy bonding (Epotek 353ND), which is then directly glued, using the same bonding, at the back of the WC base plate (Fig. 4), below the sample assembly. The ceramic disk provides electrical insulation to the transducer, as current flows through the base plate (cf. previous section). This transducer is used as an acoustic source and will be later referred as such. The top transducer (Olympus V129, P wave, 10 MHz center frequency) is glued using the same bonding material within the WC spacer located in the deformation column, above the sample's assembly (Fig. 4). Again, a 0.25 mm thick alumina disk is used to electrically insulate the transducer from the apparatus. This transducer is used as an ultrasonic receiver.

A high frequency, high voltage pulser (Eurosonic Mistras UTC-110)

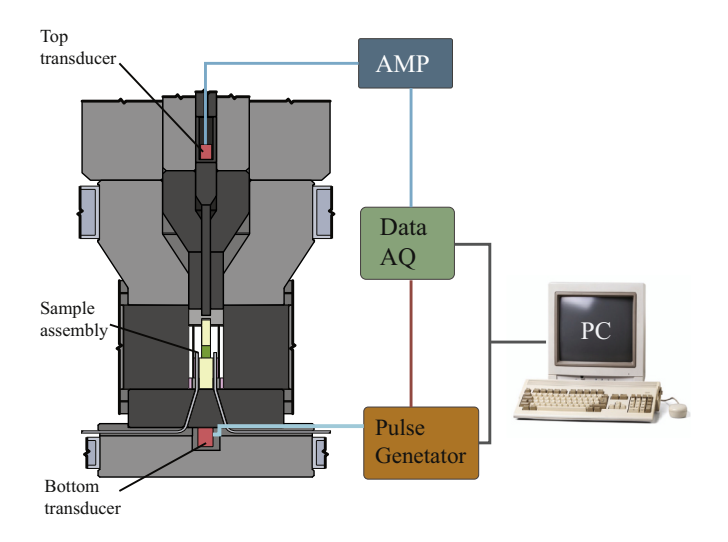


Fig. 4. Schematics of the active acoustic monitoring system.

is used to excite the acoustic source. The pulser, which is software-controlled, provides an electric pulse of 50 to 250 V amplitude, for durations of 0.05 to 0.5 μ s, at a repetition rate of up to 1 kHz. In general, 250 V pulses, with time-width of 0.1 μ s, at 1 kHz repetition rate are used. The receiver is amplified at 38 dB using a high-frequency amplifier with a flat response between 0.5 and 20 MHz.

The pulser synchronization channel, the source and the receiver are all connected via 50 Ω coaxial cables, microdot 1032 and BNC coaxial connectors to a 4 channels USB oscilloscope (Cecchi HS4, Tiepie engineering). 4096-point acoustic waveform data are recorded at a 50 MHz sampling rate, and a resolution of 12 bits, on each channel. In order to increase the signal to noise ratio, 1000 stacked waveforms are recorded

every minute during the experiment. These data are then referred to as a 'survey'. Typical waveforms obtained during an experiment are presented in Fig. 5.

Data management and pre-processing are performed using the software Insite (Applied Seismology Consulting). After each experiment, a master survey is chosen and picked manually. Arrival time differences, in reference to the master waveform, are then determined using a cross-correlation (CCR) algorithm on a 50 points (1 μ s) centered time window, interpolated at 5 ns (i.e. 200 MHz) using a spline function (Fig. 5). Resolution of the measured time difference is therefore of the order of 10 ns.

3. Experimental procedures and calibrations

Experiments in a Griggs apparatus start with a loading stage during which the pressure and temperature are increased gradually until intended P-T conditions are reached (Fig. 6). During this stage approximately hydrostatic pressure states are imposed by making sure the maximum amount of lead is maintained on top of the sample (Fig. 7).

After the loading stage, the deformation stage is initiated by keeping the confining pressure constant and setting a constant flow rate on the deformation pump to obtain a constant strain rate (cf. Section 2.2). The deformation stage includes two parts: in the first part, strain is accommodated by the lateral lead escape until there is no more lead between the sample and the alumina piston (Figs. 6 & 7). In the second part, strain is accommodated by the sample itself. The transition between those two stages is referred to as the "hit-point". The extent of sample shortening performed depends on the experiment purpose. The maximum amount of deformation available is constrained by the 5 mm course of the deformation piston, and therefore translates to maximum pure shear strains of about 50% for a 10 mm long initial sample. All experiments end with an unloading stage during which, pressure and temperature are decreased until atmospheric conditions are reached. In

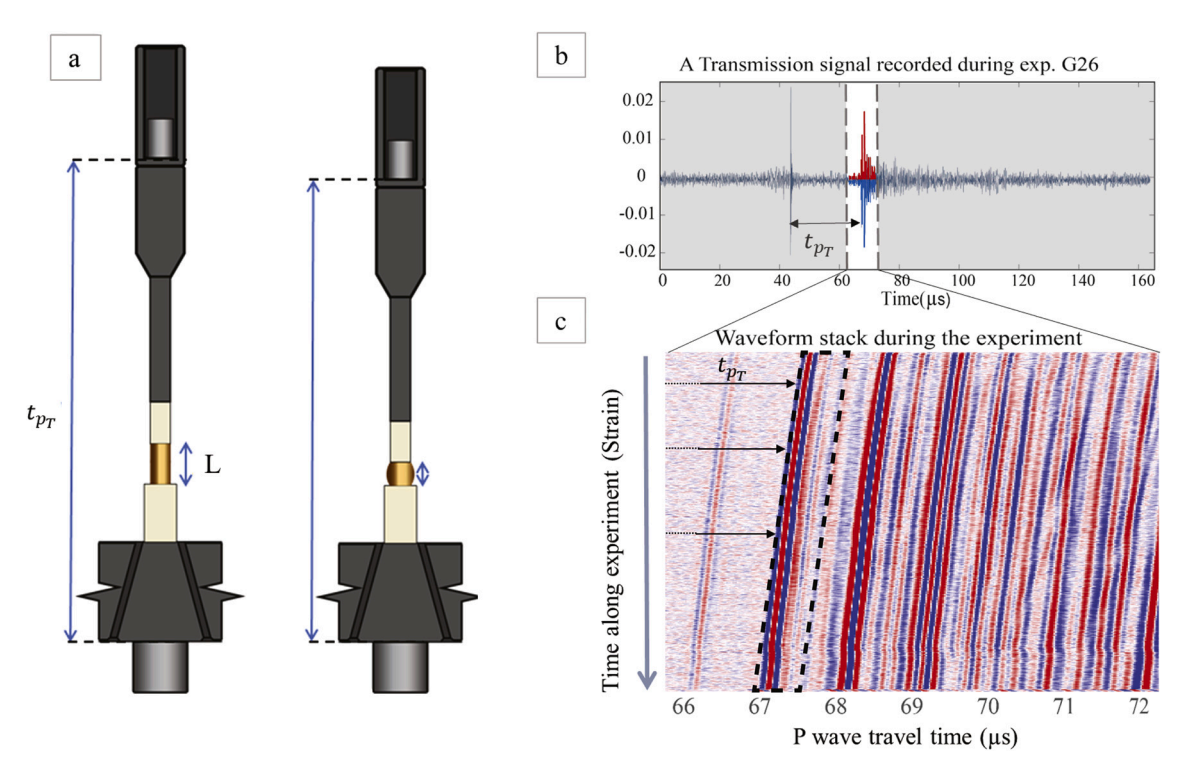


Fig. 5. a) Schematics of the P-wave travel path. During an experiment, L the sample height gets smaller because of deformation. b) Typical waveform and time of flight t_{pt} recorded by the top piezoelectric transducer. (c) Signals recorded during an experiment are plotted with red for positive amplitude and blue for negative amplitude. The time of flight t_{pt} is determined relative to that of the maser waveform (b) using a simple cross-correlation algorithm. The dashed-box represents the moving time window used during cross-correlation. (For interpretation of the references to colour in this figure legend, the reader is referred to the web version of this article.)

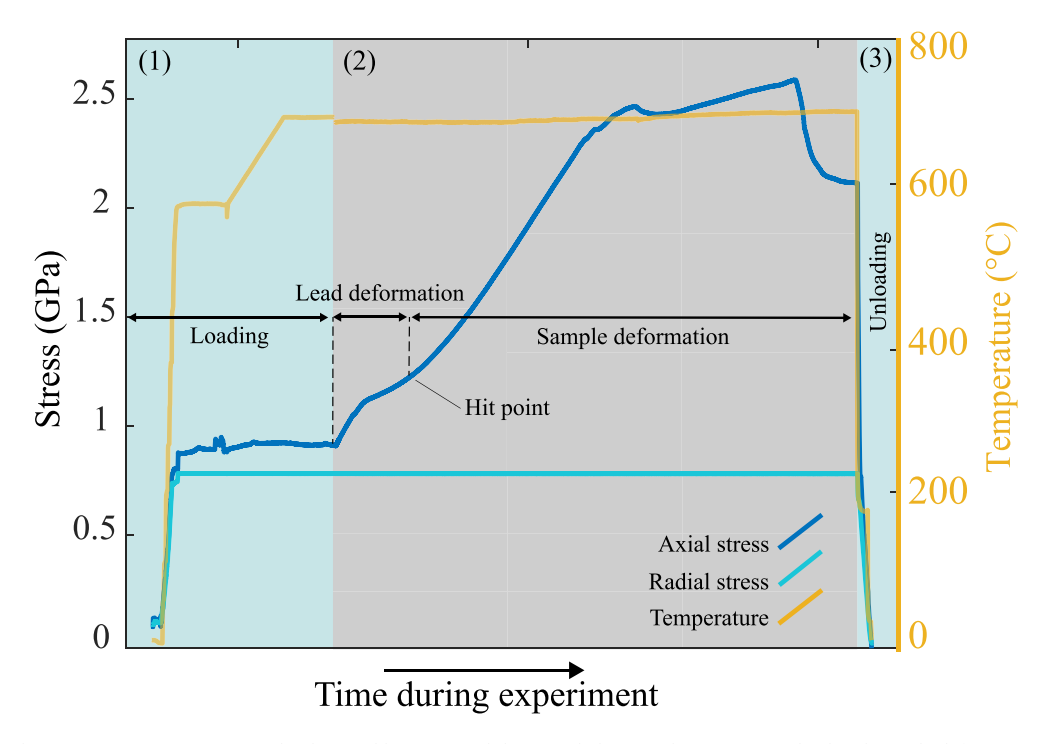


Fig. 6. Load vs. time during an experiment. Stage 1, loading and heating until the intended PT condition. Stage 2, lead and sample deformation until the yield point, Stage 3, unloading and cooling until atmospheric conditions.

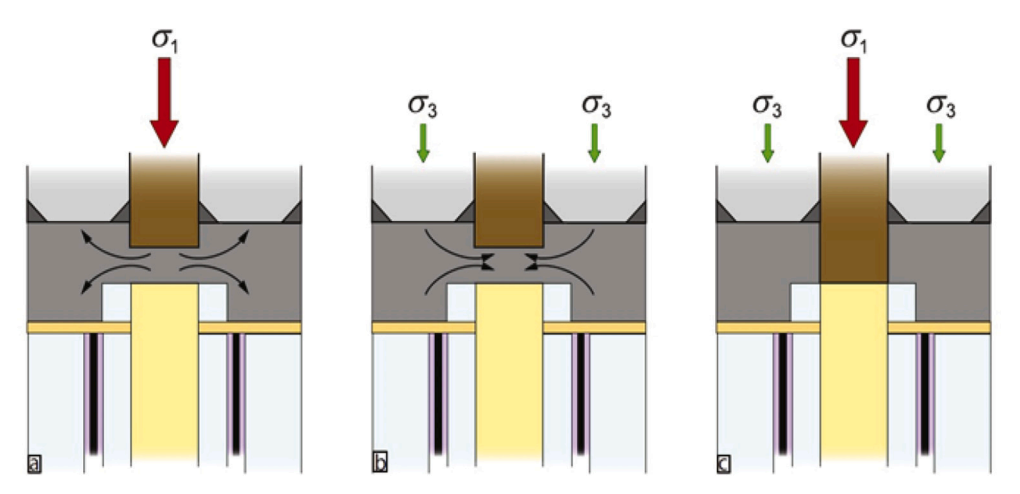


Fig. 7. Description of experimental deformation procedure, (a) the lead between alumina and WC piston flow to the outside with σ 1 and (b) flow to the inside with σ 3, (c) once σ 1 > σ 3, the lead is squeezed and two pistons are on contact and sample deformation start. Modified from [Pec et al. (2012)].

order to limit the development of decompression cracks, axial pressure is maintained higher than radial pressure during the decompression stage. In this stage, we sometimes also quench the temperature to preserve the transformation product in the sample.

3.1. Temperature calibration

A thermal numerical model was developed using Matlab to constrain the temperature distribution in the deforming cell, and the temperature gradients between the thermocouples (measured temperature) and the sample (temperature of interest). This code solves the heat equation, by using an implicit finite difference method in cylindrical coordinates (r, v, θ), with no variations of temperature in θ :

$$\rho \cdot C_p \cdot \frac{\partial T}{\partial t} = \frac{1}{r} \cdot \frac{\partial}{\partial r} \left(k \cdot r \cdot \frac{\partial T}{\partial r} \right) + \frac{\partial}{\partial y} \left(k \cdot \frac{\partial T}{\partial y} \right) + Q \tag{1}$$

where ρ is the density, C_p is the heat capacity, k is the thermal conductivity, T is temperature, r is radial distance, y is axial distance, and Q is the heat production.

The initial model configuration has been drawn to represent a 2D axial cross-section through the sample assembly, which is surrounded by tungsten carbide at the top (pistons) bottom (base platen) and sides (pressure vessel core) (cf. Figs. 2 & 3). For faster calculations, we performed simulations with a half model, as the set-up is symmetrical in the radial direction (Fig. 8). Thermocouples are not included in the model and the materials and their physical properties are listed in Table 1.

The initial temperature in the whole model is set to $T_o=20\,^{\circ}\text{C}$. The heat source in the graphite furnace elements is computed as a volumetric production (see Table 1) that represents the heat generated by Joule effect in our experiments. Temperature at the top, bottom, and outer side boundaries is fixed to 20 $^{\circ}\text{C}$. The inner side boundary is set to zero flux for symmetry reasons. The temperature field inside the sample

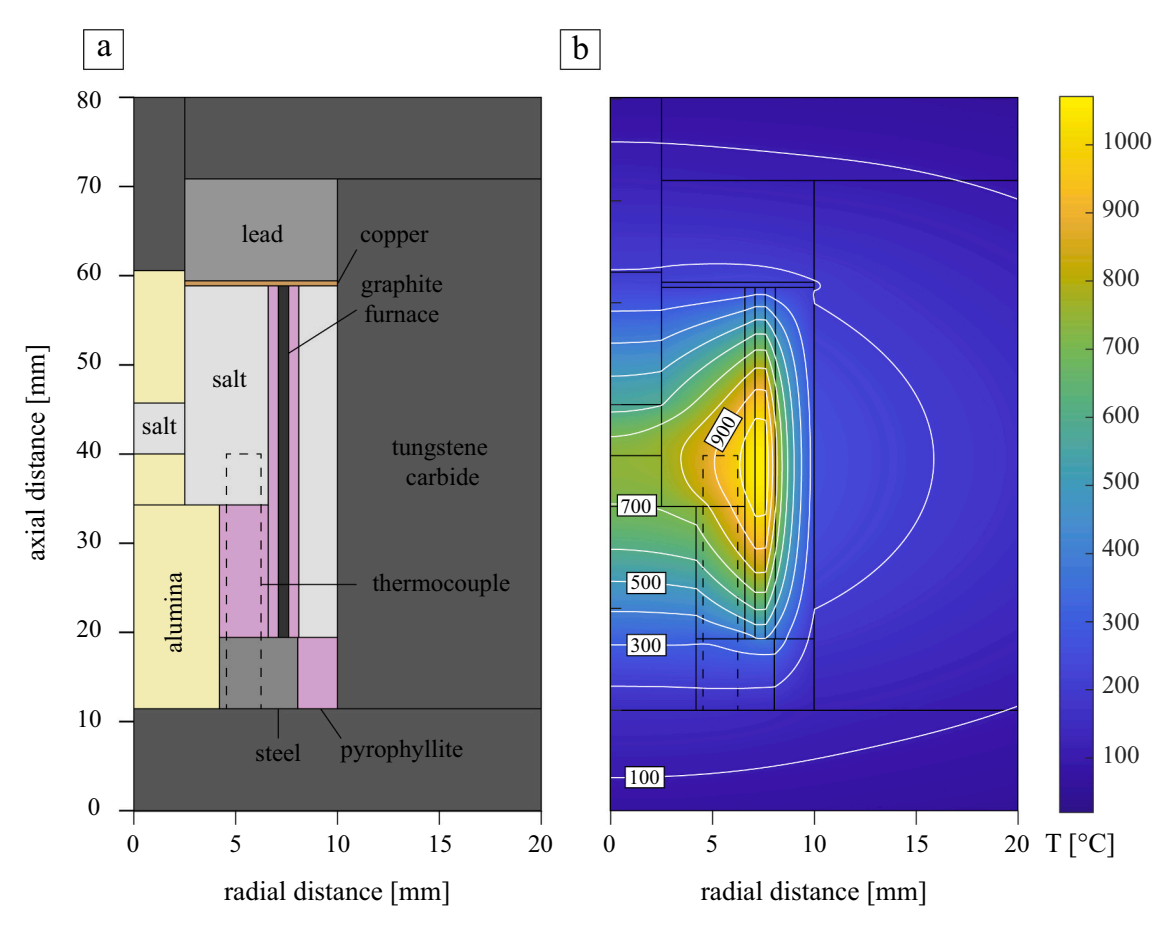


Fig. 8. Schematics of the modeled assembly (left). The simulation considers a half-assembly only. Temperature field predicted by the model inside the assembly for 1.7kWs power output. Note the important gradient and differences in temperature predicted between the graphite furnace, the thermocouples and the sample.

Table 1Physical properties and materials used for the heat diffusion model of our assembly.

Material	$ ho~[\mathrm{kg.m}^{-3}]$	C_p [J.kg $^{-1}$.K $^{-1}$]	$k \text{ [W.m}^{-1}.\text{K}^{-1}]$
Tungsten carbide	15,630	$5.12 \times 10^{1} \text{ x ln(T)} - 1.26 \times 10^{2}$	$-1.38 \times 10^{-2} \mathrm{x}\mathrm{T} + 6.17 \times 10^{1}$
Steel	8000	$-1 \times 10^{-4} \mathrm{x} \mathrm{T}^2 + 3.07 \times 10^{-1} \mathrm{x} \mathrm{T} {+} 386.69$	$2.16 \times 10^{-2} \mathrm{x} \mathrm{T} + 1.55 \times 10^{1}$
Salt	2400	$101 \times \ln(T) + 278$	$1.10 \times 10^{-11}~{\rm x}~{ m T}^4$ $-4.51 \times 10^{-8}~{ m x}~{ m T}^3$ $+~7.02 \times 10^{-5}~{ m x}~{ m T}^2$ $-5.11 \times 10^{-2}~{ m x}$
			T+ 1.66e1
Pyrophyllite	2840	6.43e2*ln(T) - 2.87e3	$6.43 \times 10^2 \text{ x ln(T)} - 2.87 \times 10^3$
		$-1.49 \times 10^{-10}\mathrm{x}\mathrm{T}^4 + 1.16 \times 10^{-6}\mathrm{x}\mathrm{T}^3$ $-3.39 \times 10^{-3}\mathrm{x}\mathrm{T}^2 + 4.58\mathrm{x}\mathrm{T}$	
Graphite	2200	3.94×10^{2}	$-6.54 \times 10^{-9} \text{ x T}^3 + 5.43 \times 10^{-5} \text{ x T}^2 - 1.49 \times 10^{-1} \text{ x T} + 1.49 \times 10^2$
Gold	21,400	$130.79 – 8.7 \times 10^{-3} \text{ x T} + 2.51 \text{ x} 10^{-5} \text{ x T}^2 – 1.91 \times 10^5 / \text{T}^2$	$(4.79 \times 10^{-4} \text{ x T} + 0.24)^{-1}$
	•		4.10×10^{-11} x T^4 - 1.90×10^{-7} x T^3 + 3.33×10^{-4} x T^2 - 2.69×10^{-1} x
Alumina	3950	$3.30 \times 10^2 \text{ x ln(T)} - 1.07 \times 10^3$	$\mathrm{T+9.19}\times10^{1}$
Copper	8960	1.07e-1*T+ 3.52e2	$-6.77 imes 10^{-2} ext{ x T} + 4.23 imes 10^{2}$
Lead	11,300	$3.22 \times 10^{-2} \text{x T+ } 120.71$	-1.59e-2*T+4e1
Heat production par	rameters		
Initial	$T_{ini} =$		
temperature	20 °C		
Output power	1.7 kW		

assembly predicted by the model is shown on Fig. 8 (right panel). For an output power of 1.7 kW, the model predicts a temperature of approximately 1000 $^{\circ}\text{C}$ in the furnace, 900 $^{\circ}\text{C}$ at the thermocouple location, and 700 $^{\circ}\text{C}$ at the center of the specimen. To confirm the important difference between the temperatures predicted at the thermocouple location and inside the sample, a calibration experiment was performed using a right-angled thermocouple (Fig. 9), with the aim of measuring the temperature at the center of sample's assembly. In this case, a cylinder of non-porous alumina replaced the lower half of the sample, while the upper part of the sample was replaced by salt. The right angle thermocouple was bent such as to measure the temperature at the center of

the assembly, at the interface between salt and alumina.

Measurements were carried out for temperatures ranging from 200 to $1000\,^{\circ}\text{C}$, and confining pressures of 0.5, 1.0, 1.5 and $2\,\text{GPa}$. Results of the calibration experiments revealed that the temperature difference between the temperature measured by both thermocouples is linear, with a ratio of 0.81 between the temperature measured at the center of the assembly, and that measured at the thermocouple location, i.e. a difference less dramatic than the 0.75 predicted by the heat-diffusion model. A recent run, including both the presence of metal thermocouples and temperature dependence of conductivity, density and heat capacity for salt (and pyrophylite using talc as a proxy) showed that the

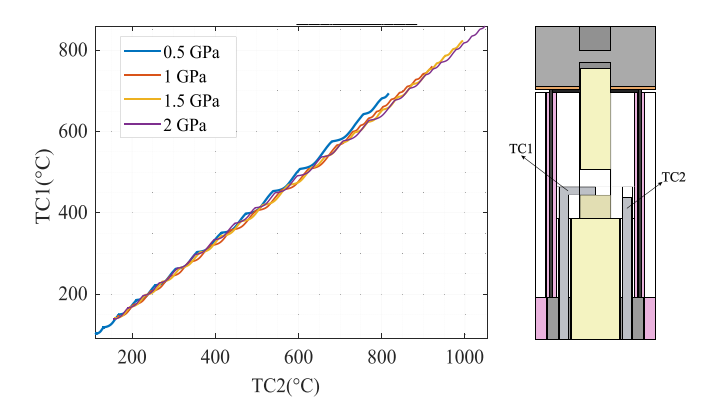


Fig. 9. Left. TC2 vs. Tc1 (right- angled thermocouple) at 0.5, 1, 1.5 and 2 GPa hydrostatic pressure, and within the range 200–1000 °C. Right. Sketch of the modified sample assembly used for temperature calibration. The small oscillations on these curves are the result of the system being used in output power mode. Indeed, after each increase in output power, the temperatures within the sample assembly stabilized only after 5–10 min (maybe because of efficient cooling of the vessel).

difference was smaller (0.88 instead of 0.75) when these are taken into account, but still comparable to the one measured experimentally (0.81). This value is similar to the 0.9 measured experimentally by (Kirby and Kronenberg, 1984), albeit between a right-angle thermocouple placed on the side of the specimen and thermocouple placed in the center of the sample assembly. In the following, all the measured temperatures reported in text and figures have been corrected using the 0.81 linear ratio.

3.2. Hit-point determination

The hit-point represents the beginning of sample deformation, when the lead has completely escaped the gap between the alumina and WC pistons (Fig. 7). It can be determined using both mechanical and active (pulse-transmitted) acoustic data.

The lead flow-strength is significantly lower than that of the sample elastic strength, so the mechanical hit point is defined by an increase of the slope in the axial stress - axial shortening (time) curve. In practice, the hit-point is determined as the intersection of the two linear approximations corresponding to the viscous drag due to lead flow on the one side and the sole elastic loading of the column on the other side (Fig. 10). Resistance of the assembly to lateral escape of lead is possibly responsible for the significant hardening during lead flow. A change in slope in the travel-time shift – (experimental) time is also observed at the

hit-point (Fig. 10). Indeed, the P-wave velocity in lead is approximately ≈ 2 km/s, i.e. significantly lower than in the rest of the axial column (\approx 6.3 km/s), the progressive lateral escape of the lead from the loading column induces an increase in the apparent column velocity (see Section 3.4).

These two independent determinations of the hit-point allow for an estimate of the uncertainty on its exact position. Curves on molybdenum and nickel show a \pm 50 MPa uncertainty on the hit-point position along the differential stress $(\sigma_1$ - $\sigma_3)$ axis, and therefore the same systematic uncertainty for differential stress when counted from the hit point reference. The hit-point in this study is determined from the differential stress curve and in the following, both the differential stress $(\sigma_1$ - $\sigma_3)$ and the axial shortening will be evaluated relative to hit-point.

3.3. Apparatus (mechanical) stiffness calibration

As described previously, the load column includes several parts, which deform elastically when stress is applied. Therefore, the displacement measured by LVDTs during our experiments also includes elastic shortening of the load-column, proportional to the applied force, i.e. to the apparatus stiffness Km (N/m).

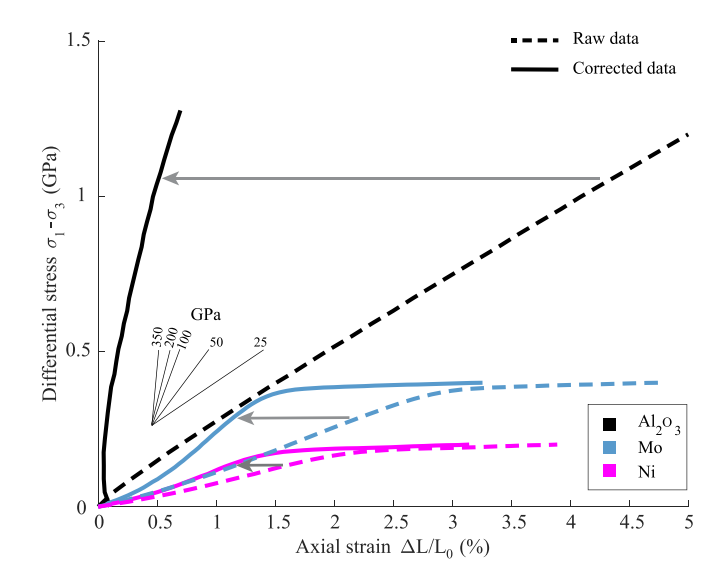


Fig. 11. Stress vs. strain for alumina, molybdenum, nickel and quartz. Dash lines represent non-corrected data and solid lines represent corrected strain in %. Inset represents Young's modulus trajectories.

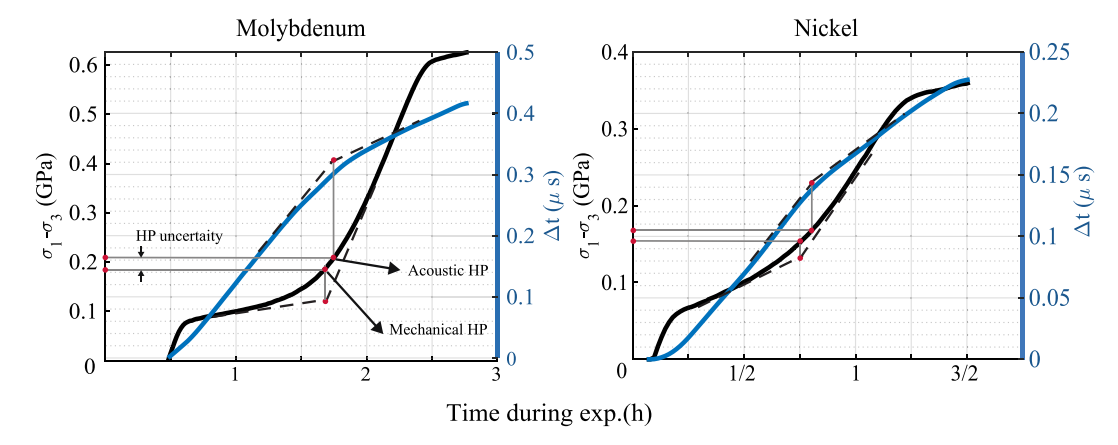


Fig. 10. Hit points for two experiment performed on molybdenum (left) and nickel (right). The hit point is defined as the intercept between lead deformation and elastic loading of the sample. The left axis corresponds to the differential stress vs. time record (black curve) and the right axis corresponds to the acoustic travel time shift vs. time record. Both hit-points differ slightly and in the following the traditional differential stress vs. time (strain) hit-point was used.

In order to measure the stiffness of the load-column, several calibration experiments were performed at different P-T conditions (Fig. 11).

First, a sample of non-porous alumina was used for calibration experiments (at 1.5 GPa & 700 °C) so that the whole column behaves elastically The raw stress-strain curve observed with an alumina sample is indeed linear (Fig. 10) and yields an elastic loading curve slope of 25 GPa corresponding to the overall elastic strength of the various parts composing the column. However, if the Young's modulus of alumina, in these P-T conditions, is set to 350 GPa, as expected for A1 grade Al2O3 ceramic at 500 °C (Shimada et al., 1984) for the first deformation increments (up to 0.5 GPa differential stress and 0.17% strain), then the true shortening of the sample dl, can be estimated. The apparatus stiffness compliance K_m and the sample shortening dl are related:

$$dl = \frac{\sigma_1 - \sigma_3}{E_{A/2O3}} = \Delta L_R - \frac{F}{K_m}$$
 (2)

where dl and ΔL_r (mm) are the corrected and raw displacements, $\sigma_1+\sigma_3$ (Pa) is the differential stress, E_{Al2O3} (Pa) the Young's modulus of alumina and F (N) the applied (differential) load. From that calibration experiment, we obtain a value for the stiffness of $K_m=52$ kN/mm (or apparatus compliance $k_m=\frac{1}{k_m}=19$ µm/kN). Because this calibration does not take into account the possible deformation of the middle-platen (see Fig. 3, Burdette and Hirth, 2020) during the test, we should consider it as valid for 'isobaric' conditions only, i.e. when the confining pressure remains constant. A set-up using two LVDTS mounted on the bottom and middle platen as in (Rybacki et al., 1998) could help determining the apparatus stiffness linked to a change in confining pressure.

This calibration was validated using molybdenum and nickel samples (similar to that of (Holyoke and Kronenberg, 2010; Kido et al., 2016) at 0.5GPa and 500 °C and a strain rate of $\approx 10^{-5}/\,\mathrm{s}$. The difference between stiffness corrected stress-strain curves and the non-corrected ones are displayed on Fig. 11. Arrows highlight the impact of stiffness correction on our data, the magnitude of which increases with sample strength. Note that the correction has no impact on the flow stress, but lowers the axial strain needed to reach plastic flow.

3.4. Acoustic stiffness calibration

The most challenging part of acoustic monitoring is calibration. As described above, two high frequency (5-10 MHz) piezoelectric transducers are used for active acoustic monitoring. During deformation, the distance between the top and bottom transducers changes (Fig. 5a) and as a consequence, so does the time of flight t_{pt} between the two (Fig. 5b). The typical evolution of t_{pt} during an experiment is displayed on Fig. 5c, where the x-axis is travel time, the y-axis is time during the experiment and the colour scale gives the amplitude of the acoustic signals (red = positive, blue = negative). One can clearly see the shift in travel time as the sample is shortened. t_{pt} may vary because of three combined contributions: 1) a change in sample length; 2) a change in velocity within the sample itself, and finally 3) a change in column length due to elastic loading (or unloading), a contribution that needs to be accounted for.

To account for the first two contributions, let t be the travel-time though a sample of length L and velocity V. The three quantities are related via: L = V t. dt is therefore the change in travel time (further on referred as time shift), dL is the shortening, dV is the velocity evolution, all three within the sample only. The time shift is the combination of the respective effects of the sample shortening dl/L and of the velocity change dv/V within the sample:

$$\frac{dt}{t} = \frac{dl}{L} - \frac{dv}{v} \tag{3}$$

In such a way, in the absence of velocity change (dv = 0) within the sample, the P-wave velocity can be obtained from the time shift dt and the sample shortening dl only, i.e. V = dl/dt, once the contribution of the

elastic shortening of the column is accounted for.

For practical purposes, we measure the time shift $\Delta t_{\rm raw}$ by cross-correlation of signals relative to the signal obtained at the hit point, which serves as a reference. The time shift due to elastic deformation of the column must be proportional to the applied load so that the true time shift dt, the measured time shift $\Delta t_{\rm raw}$ and the applied load F [kN] are related as follows:

$$dt = \Delta t_{raw} - \frac{F}{K_a} \tag{4}$$

where Ka is an 'acoustic stiffness' [kN/ μ s]. We will note Vm = Ka/Km the apparent wave speed of the loading column [mm/ μ s \equiv km/s].

In order to measure K_a , several calibration experiments were performed with materials (nickel, molybdenum and lead) for which the room temperature P wave velocity is known (Fig. 12).

Fig. 12 compares the corrected shortening vs. time shift curves with raw data. Minimizing the error on the estimate of P wave velocities in lead, nickel and molybdenum yields an acoustic compliance $k_a=1/K_a=0.003~\mu s/kN$, P-wave velocities at 0.5 GPa and 500 °C were fitted along the dashed portion of the curves to be of 2.2, 5.05 and 5.6 km/s for lead, nickel and molybdenum respectively, to be compared to 2.2, 5.6 and 6.2 km/s at room pressure and temperature.

Note that the value of acoustic compliance k_a also yields an apparent P-wave velocity of the loading column $V_m = k_m/k_a = 6.3$ km/s, equal to that commonly reported for tungsten carbide, a material which constitutes close to 75% of the travel path between the two transducers (see Fig. 11). Finally, these reported values for k_a , k_m and V_m are the ones expected for a column made of 100 mm WC and 40 mm Al_2O_3 , with respective Young's moduli of $E_{WC} = 600$ GPa and $E_{Al_2O_3} = 200$ GPa and velocities of $Vp_{WC} = 6.2$ km/s and $Vp_{Al_2O_3} = 10.5$ km/s.

3.5. Thermal expansion of the column

Finally, a reference experiment was performed to estimate the isobaric thermal expansion of the loading column. For this experiment, an alumina cylinder was used as a sample at 1 GPa and the temperature was increased from 200 to 900 °C, before hit-point, and while maintaining the hydrostatic pressure constant. The measured thermal expansion of the column during this heating cycle was constant, equal to $\approx 10^{-3}$ mm/K, with a corresponding time-shift of $\alpha_a = 4 \times 10^{-4}$ µs/K, which yields an apparent column velocity of $V_c = 2.5$ km/s upon heating

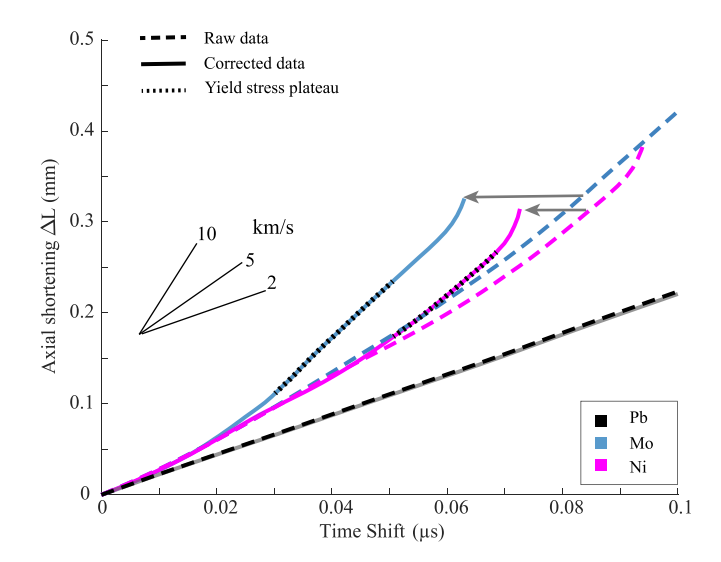


Fig. 12. Axial shortening vs. time shift for molybdenum, nickel and lead. Dashed and solid lines represent non-corrected data and corrected time-shifts, respectively, i.e., $\Delta t_{\rm raw}$ and dt in 948 Eq. (4), respectively. Inset represents trajectories for different values of the P-wave velocity.

under hydrostatic conditions. This value for apparent velocity highlights that lead flowing inside or outside the loading column accommodates most of the travel-time shift. Consequently, an additional correction to the time-shift is needed due to the expansion of the column upon temperature change during an experiment:

$$dt = \Delta t_{Raw} - \alpha_a \Delta T \tag{5}$$

where α_a is the 'acoustic' thermal expansion of the column (µs/K) and ΔT the temperature change relative to the reference value. The absolute velocity within the sample may then be calculated using:

$$V_p = \frac{L_0(1 + \alpha \Delta T)}{t_0 - dt} \tag{6}$$

with L_0 the sample initial height, α the thermal expansion coefficient of the sample material, ΔT the change in temperature and $t_0 = L_0/V_0$, where V_0 is obtained from a thermodynamics database such as that of (Abers and Hacker, 2016).

3.6. Uncertainty on our measurements

As previously presented, several calibration methods are used in order to obtain precise measurements. From the difference between acoustic and mechanical hit-point, we have an uncertainty of about ± 50 GPa on our stress measurements. Using alumina as a primary standard, we obtained a load column stiffness Km=52 kN/mm. This calibration allows us to fit the alumina.

Young's modulus at the beginning of loading which correspond to the elastic stage (Fig. 10). We cannot fit Young's modulus of molybdenum and nickel because determination in these experiments is not purely elastic. However, our corrected data, compare well with those of (Holyoke and Kronenberg, 2010; Kido et al., 2016) (Fig. 13) who compiled experimental data on the deformation of Nickel and Molybdenum, in similar conditions (300 MPa, 600 °C, 2×10^4 /s), using either a gas or a Griggs apparatus, in the latter case using either solid salt and molten assemblies. The data shows that the resolution in differential stress of our Griggs apparatus, using a solid salt assembly, is comparable to that of former generations, of the order of 50 MPa. Note that one important contribution to uncertainties in our measurement of differential stress is the friction between the deformation piston, the mitre ring and the sample's assembly (Pec et al., 2012). The best way to correct for friction within a Griggs apparatus remains under debate (Heilbronner et al., 2020) and hence was not taken into account in this study.

However, depending on pressure and temperature conditions, one can expect a discrepancy ranging between 10, and as much as 30%, between the value of differential stress measured by the load cell after hit-point determination and its true value.

Using lead as primary standard for P wave velocity, we tuned acoustic compliance k_a to 0.003 $\mu s/kN$ to fit the sound velocity for lead. Lead has been chosen to take advantage of the unequivocal linear first order effect of lead extrusion on the time flight data (Fig. 12). Although pressure and temperature derivatives for lead are not known in the solid domain, its relatively limited density variation from 0 to 500 $^{\circ} C$ (about 1% for alpha $=29.\ 10^{-6}\ K^{-1})$ allows to use the 2.16 km/s atmospheric condition P-wave velocity as a reference. Using this, P-wave velocities of.

5.05 and 5.6 km/s were estimated for Mo and Ni, used here as secondary standard for error estimates. Using standard velocity values and temperature-related partial derivatives for these two metals (Chen, 2011; Dickinson and Armstrong, 1967) P-wave velocities for these two metals at $500\,^{\circ}$ C are estimated at $6.12\,$ and $5.53\,$ km/s for Mo and Ni, respectively. Pressure effects are neglected due to their second order effect (Duffy and Ahrens, 1994). The error in Vp is therefore -16% for Mo and -8% for Ni. Our apparatus generally tends to systematically underestimate velocities but with less than 15% error in absolute value. This can be explained by the effects of interfaces acting as slow domains along the wave path. However, we believe our error in relative elastic wave velocity evolution (ie. dv/v) is much lower than the 10% above mentioned, capable of detecting changes in velocity in the sample of the order of $0.1\,$ km/s.

4. Experimental results

4.1. Evolution of P-wave velocities during the deformation of quartz

In order to test the consistency and stability of the P wave velocity determination system on mineral aggregates, four deformation experiments were done on samples of dry samples of Arkansas Novaculite (grainsize 5–10 μ m), in the α -quartz P-T domain at 725 °C, confining pressures of 0.75, 1 and 1.5GPa, and strain rates of 10^{-6} /s, 5×10^{-6} /s and 10^{-5} /s (Fig. 14). Corrected differential stress (σ_1 - σ_3) versus axial strain curves show a typical elastic to plastic behavior, with an apparent Young's modulus close to 50 GPa. Our yield stress values are comparable to those reported by Hirth and Tullis (1994), who reported semi-brittle behavior in Heavytree quartzite, a material with much larger grainsize (200 μ m), under similar pressure, temperature and strain rate

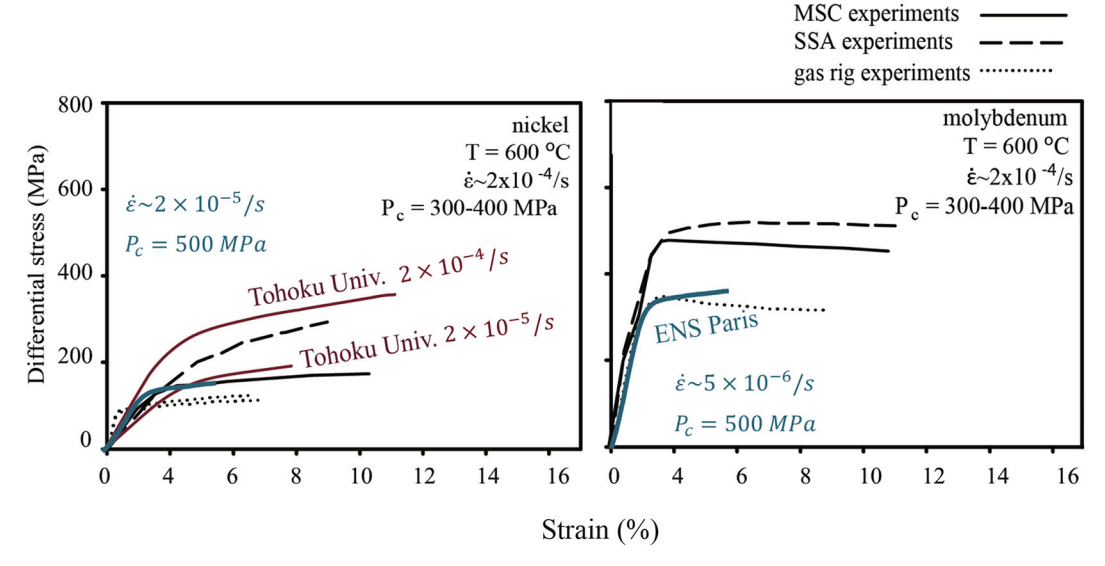


Fig. 13. Corrected stress-strain curves for molybdenum and nickel, compared to available data by Holyoke and Kronenberg (2010) and Kido et al. (2016).

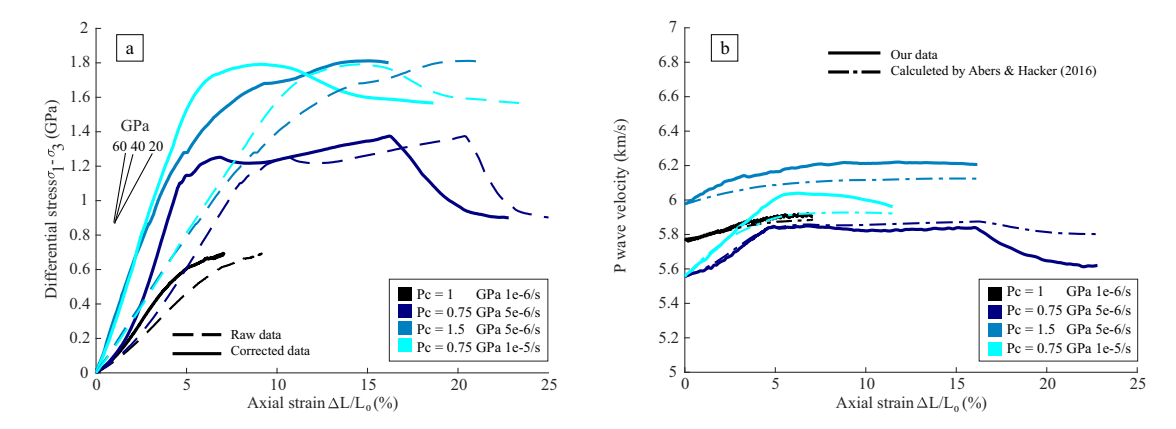


Fig. 14. (a) Differential stress vs. axial strain during the deformation of cored samples of Arkansas Novaculite (5 μ m grain size, 99% pure quartz), at T = 725 °C. Pc = 0.75, 1 and 1.5 GPa, and strain rates ranging from 10 to 6/s (at 1GPa), to 5 \times 10–6/s (1.5 and 0.75 GPa) and 10–5/s (0.75GPa). Dashed curves are raw data (i.e. before stiffness correction). Inset gives Young's modulus trajectories for E = 20, 40 and 60GPa. (b) P-wave velocity vs. axial strain during the same experiments. Solid lines represent the velocities calculated from our experiments and dashed-linear represent the velocities calculated using Abers and Hacker (2016) algorithm with pressure equal to effective mean stress P = $(\sigma_1 + 2\sigma_3)/3$.

conditions. For instance, the yield stresses of 1.2 to 1.8 GPa we measured at $T=725\,^{\circ}\mathrm{C}$ are comparable to the value of 1.75 MPa they reported for $T=700\,^{\circ}\mathrm{C}$, P=0.8 GPa, and $10^{-5}/\mathrm{s}$. Our results highlight the pressure dependence of yield stress of quartz, which, at a strain arte of $5\times10^{-6}/\mathrm{s}$, increases from 1.2 GPa to 1.8 GPa at 0.75 GPa and 1.5 GPa confinement respectively. This pressure dependence is compatible with the observations of Hirth and Tullis (1994). They observe a yield stress going from 1.14 to 1.5 GPa, with 0.75 GPa and 1.2 GPa confinement pressure respectively and both at 700 °C with the strain rate of $5\times10^{-6}/\mathrm{s}$. Finally, our observations also highlight the important strain rate dependence of quartz strength under these relatively cold conditions, with a yield stress of 0.7 GPa at the slowest strain rate tested ($10^{-6}/\mathrm{s}$), again comparable to observations performed by (Hirth and Tullis, 1992) on Heavytree quartitze ($\sigma_y=800$ MPa at 1.5 GPa, $700\,^{\circ}\mathrm{C}$ and $10^{-6}/\mathrm{s}$) or Novaculite ($\sigma_y=600$ MPa at 1.5 GPa, $700\,^{\circ}\mathrm{C}$ and $10^{-6}/\mathrm{s}$) but 0.17 wt% water added).

The right panel of Fig. 14 shows the evolution of P-wave velocities during deformation for the four experiments. Velocities were calculated using the formula: $V_p = (L_0 - dL)/(t_0 - dt)$ with L_0 the sample initial height, dL the corrected shortening, dt the corrected time shift calculated by cross-correlation according to Eq. (4) and $t_0 = L_0/V_0$, where V_0 is the velocity at P,T conditions, before deformation, obtained using the

database of (Abers and Hacker, 2016). The figure compares the evolution of our velocity measurements (solid lines) with the prediction of Abers and Hacker (2016), using effective mean stress values $(\sigma_1+2\sigma_3)/3$ measured in the experiments as pressure values in the Abers and Hacker (2016) computing toolbox. Our measurements and the prediction of Abers and Hacker (2016) remain close to one another within 0.1 km/s during the entire range of the experiments. Though measurements are somewhat higher than predictions, particularly at the fastest strain rate. Nevertheless, our measurements tend to systematically overestimate increase in P-wave velocity, which is particularly clear for the experiment performed at fastest strain rate. This discrepancy could be due to an acoustoelastic effect recently described in olivine by Traylor et al. (2019).

4.2. Evolution of P-wave velocities at the $\alpha \to \beta$ quartz phase transition

In order to test the sensitivity of the active acoustic monitoring system to measure sample P-wave velocity, the $\alpha\to\beta$ quartz transition has been chosen for its instantaneous kinetics and its theoretical sharp signature in P wave velocity (Abers and Hacker, 2016). Arkansas Novaculite was used for hydrostatic pressure experiments at 0.5 and 0.8 GPa which gradually increasing the temperature from 200 to 900 °C

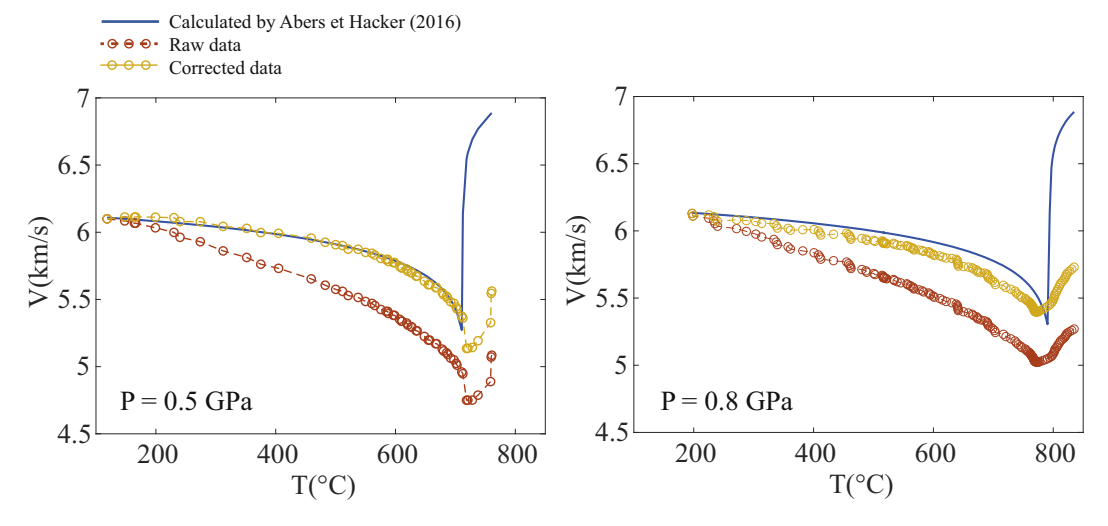


Fig. 15. P wave velocity vs. temperature for two experiments at Pc = 0.5 GPa (left) and 0.8 GPa (right) hydrostatic pressure performed on Arkansas Novaculite. Red and yellow lines are raw and corrected data, respectively. Solid lines are velocity trajectories calculated for pure quartz using Abers and Hacker (2016). (For interpretation of the references to colour in this figure legend, the reader is referred to the web version of this article.)

(Fig. 15), in order to cross the transition. During such experiments, a negative displacement of the deformation ram is observed, due to the thermal expansion of the loading column while maintaining a constant confining pressure. (nb: For an increase of 700 °C in temperature, the thermal expansion of our quartz sample is less than 0.1 mm, which cannot account for the observed displacements). Using Eqs. (5-6), the corrected Temperature - velocity (Fig. 15) curves for two experiments performed at 0.5 and 0.8 GPa hydrostatic pressure are compared to the velocity curves calculated by Abers and Hacker (2016). At both confining pressures, we observe a decrease (i.e., a softening) of the velocity with increasing temperature. The magnitude of this softening phase increases approaching the $\alpha \rightarrow \beta$ quartz phase transition and is comparable to that expected from the thermodynamic database of Abers and Hacker (2016). The temperature at which the transition is observed is in remarkable agreement with the predicted temperature. These crucial observations prove the reliability of our measurements and applied corrections. We see an increase of the transition temperature with pressure, from 718 °C at 0.5 GPa, to 769 °C at 0.8 GPa, which yields an experimental determination of Clapeyron slope of the transition of 5.9 MPa/K, or 0.17 K/MPa, to be compared with values ranging between 0.214 and 0.26 reported by various studies (Bagdassarov and Delépine, 2004). This last point suggests that we either might be overestimating the temperature correction, or maybe that the transition is not linear in P-T space as previously suggested by (Mirwald and Massonne, 1980;

However, only a slight increase in Vp is observed at temperature beyond the transition, in disagreement with the sharp change in velocity predicted by (Abers and Hacker, 2016), and measured experimentally (Kern, 1982; Zappone and Benson, 2013), albeit at lower pressure. The causes of this discrepancy, may be due to experimental artifacts such as a strong thermal gradient in our sample or micro-cracks induced by the structural transition (Glover et al., 1995; Johnson et al., 2021), or possibly inaccurate thermodynamic databases.

5. Perspectives for geological and geophysical interest

Acoustic properties of natural aggregates are controlled to first order by the elastic properties of their constituting mineral phases, their textures and the presence of fluid. Active acoustic monitoring of deformation experiments is a promising tool to (1) explore how in-situ acoustic properties are impacted by strain and metamorphic reactions and (2) establish the seismological signature of these transformations at larger space scales and lower wave frequencies.

Some metamorphic reactions or phase transitions, have a large enough acoustic signature to be directly detected in the geophysical signal. For instance, the $\alpha \to \beta$ quartz transition, is associated with a V_p change of about 1.1 km/s at 900 °C in pure quartz and a 0.3 to 0.5 km/s change in granite with 30% quartz (Mechie et al., 2004). The displacive nature of the phase transitions limits the depth range over which quartz turns from β to α with increasing pressure to a few hundred meters, hence generating a sharp impedance contrast visible both in tomography (Mechie et al., 2004) and receiver functions and attenuation (Sheehan et al., 2014).

Drastic change in Poisson's ratio in the vicinity of the reaction, due to change of sign of stiffness constants, is also expected to have an impact on geophysical signatures (Pimienta et al., 2018).

Such features have been used in geophysics to estimate temperatures at depth, based on (1) an assumption on the local geotherm, to estimate at what temperature the reaction is crossed, and (2) the assumption that the phase reaction is solely controlled by temperature and hydrostatic pressure, to relate pressure to depth. Even though low confinement experiments on the $\alpha \to \beta$ transition (Coe and Paterson, 1969) show that the mean stress (pressure stricto sensu) controls the reaction, the extrapolation of this result to natural pressures must still be confirmed. Comparable experiments on the quartz-coesite transition at higher confining pressures (Ji and Wang, 2011; Richter et al., 2016) for

instance, show a more complex interaction between stress state and reaction. Active acoustic monitoring is a promising tool to investigate these questions. While the transient decrease in Young's Modulus in the vicinity of the reaction (Peng and Redfern, 2013; Westbrook, 1958) is expected to be seen in the strength record (hence providing an independent estimate on the reaction occurrence), velocity changes of 5% are well above the sensitivity estimated for our device. Any deviation or offset from theoretical values could reveal reaction-induced self-cataclasis (Glover et al., 1995; McKnight et al., 2008) Dauphiné twinning effects (Menegon et al., 2011) or possibly, the occurrence of incommensurate transient phase (Dolino et al., 1984). Such experiments could also yield direct evidence of the strain localization within quartz aggregates when crossing their $\alpha \rightarrow \beta$ transition such as deduced from internal friction estimates from mechanical spectroscopic investigations (Nikitin et al., 2007).

Another first order velocity change that can be investigated using our device is partial melting, the occurrence of which is deduced from Vp/Vs ratio or attenuation studies, such as applied beneath the Himalayas (Kind et al., 1996; Shapiro, 2004) and the Altiplano (Schilling et al., 2006). The interpretation of velocity change in terms of partial melting is not unique as the anomaly could be affected by the presence of micas, and depends on the exact shape of melt inclusions (Hacker et al., 2014). The topology of partial melting has a direct impact on the bulk velocity of the rocks (Takei, 2017). Progressive deformation during partial melting may allow us to explore the complex interaction between deformation, melt production, drainage and fluid collection by their signature on active acoustic monitoring measurements. Pairing the acoustic data with mechanical data will help to solve these complexities. So far, the weakening effect of partial melting has only been correlated to partial melting rates and critical thresholds have been determined solely on the basis of post-mortem analysis. Independent and synchronous estimates of partial melting rates and measure of aggregates strength are required, facilitate by acoustic velocity measurements.

Third, dehydration reactions of phyllosilicates, such as serpentine group minerals, are also expected to produce important elastic wave velocity anomalies at depth and produce regions with anomalous Vp/Vs ratios (Kato et al., 2010; Kodaira, 2004; Peacock et al., 2011) because of the conjunction of high pore fluid pressure and dehydration induced micro-cracking (Pimienta et al., 2018; Wang et al., 2012). Experimental data on (Popp and Kern, 1993), the topic are uncommon at present, and our device should enable many new measurements, including P-wave and S-wave velocities and Vp/Vs ratios.

6. Conclusions

We presented a third generation Griggs type apparatus installed at the Laboratoire de Géologie of ENS Paris. Assembly preparation, and mechanical and acoustic set-up were explained in detail along with pressure and temperature calibrations. Uncertainties in stress measurement is on the order of ± 50 MPa, temperatures are known to $\pm 20~^{\circ}\text{C}$, and absolute P-wave velocities are measurable to 10%, with relative velocity changes measurable to with a few % (ie. 0.1 km/s). Experiments on dry Arkansas Novaculite have demonstrated the sensitivity of P–wave elastic wave velocities to phase changes and deformation.

Our *Griggs* apparatus with acoustic monitoring opens a wide field of possible investigation to understand the mutual impact of deformation and metamorphic reactions at lower crust and upper mantle conditions, at laboratory timescales. For instance, the $\alpha \to \beta$ quartz transition, investigated here as a test for our system, is also an important geobarometer commonly used in large scale geophysical imaging (Mechie et al., 2004; Sheehan et al., 2014).

Metamorphic reactions with a significant elastic property change or volume change could all be good candidates for an in-situ velocity study. For example, the present method should be able to detect *syn*-deformation partial melting with applications to geophysical signatures of partial melting (Kind et al., 1996; Shapiro, 2004), and mechanical

behavior of partial melts (Rosenberg and Handy, 2005), and more complex eclogitization reactions that give rise to velocity rises in the mantle (Ringwood and Green, 1966; Wittlinger et al., 2009) and strain localization (Austrheim and Griffin, 1985) in subducting slabs.

Additional experimental developments could include the combined measurements of P-wave, S-wave velocities and Vp/Vs ratios, by combining pulse-echo and pulse transmission techniques. Finally, since the pioneering works of (Mogi, 1962), piezo-ceramics have also been commonly used by the experimental rock mechanics community in passive (i.e. listening mode) applications to detect and locate acoustic emission, (i.e. high frequency elastic waves emitted by the dynamic propagation of micro-cracks) in rocks (Lockner et al., 1991; Scholz, 1968). The same technique has been successfully applied to the detection of dislocations and dislocation avalanches in ice (Weiss and Grasso, 1997) or the detection of mineral phase transitions at high-pressure (Meade and Jeanloz, 1989). Acoustic emission system has already been developed within Griggs-type apparatus (Green et al., 1992; Okazaki and Hirth, 2016), including recently on a system of the same generation (Ghaffari and Pec, 2020). Gasc et al. (2021) have recently developed this technique within our system in order to further understand the generation of deep focus earthquakes by olivine phase transitions.

Declaration of Competing Interest

None.

Acknowledgments

The development of this new generation *Griggs* apparatus could not have been achieved without the invaluable help and advice of the late Prof. Harry W. Green II. The authors would also like to thank the editor Prof. Ramon Carbonell, Prof. Pamela Burnley and Prof. Andreas Kronenberg for their constructive reviews and comments, which greatly helped improved this manuscript. Prof. Andreas Kronenberg also provided the molybdenum and nickel samples used for the cross-calibration of our apparatus. The European Research Council funded this work through grant #681346 REALISM.

References

- Abers, G.A., Hacker, B.R., 2016. A MATLAB toolbox and Excel workbook for calculating the densities, seismic wave speeds, and major element composition of minerals and rocks at pressure and temperature: Matlab and excel tools for rock wave speeds. Geochem. Geophys. Geosyst. 17, 616–624. https://doi.org/10.1002/ 2015GC006171.
- Austrheim, H., Griffin, W.L., 1985. Shear deformation and eclogite formation within granulite-facies anorthosites of the Bergen Arcs, western Norway. Chem. Geol. 50, 267–281. https://doi.org/10.1016/0009-2541(85)90124-X.
- Bagdassarov, N.S., Delépine, N., 2004. α-β Inversion in quartz from low frequency electrical impedance spectroscopy. J. Phys. Chem. Solids 65, 1517–1526. https:// doi.org/10.1016/j.jpcs.2003.10.075.
- Birch, F., 1960. The velocity of compressional waves in rocks to 10 kilobars: 1.
- J. Geophys. Res. 65, 1083–1102. https://doi.org/10.1029/JZ065i004p01083. Birch. F., 1961. The velocity of compressional waves in rocks to 10 kilobars: 2.
- J. Geophys. Res. 66, 2199–2224. https://doi.org/10.1029/JZ066i007p02199
- Bridgman, P.W., 1912. Thermodynamic Properties of Liquid Water to 80° and 12000 Kgm. Proc. Am. Acad. Arts Sci. 48, 309. https://doi.org/10.2307/20022832.
- Bridgman, P.W., 1914. The Technique of High pressure Experimenting. Proc. Am. Acad. Arts Sci. 49, 627. https://doi.org/10.2307/20025490.
- Burdette, E., Hirth, G., 2020. Enhanced dehydration weakening of antigorite driven by slow shear heating: insights from high-pressure experiments with a modified apparatus stiffness. J. Geophys. Res. Solid Earth 125. https://doi.org/10.1029/ 2020.JB020064.
- Chen, X.R., 2011. Thermoelastic properties of nickel from molecular dynamic simulations. J. At. Mol. Sci. 2, 10–19. https://doi.org/10.4208/ jams.310810.200910a.
- Christensen, N.I., 1979. Compressional wave velocities in rocks at high temperatures and pressures, critical thermal gradients, and crustal low-velocity zones. J. Geophys. Res. Solid Earth 84, 6849–6857. https://doi.org/10.1029/JB084iB12p06849.
- Coe, R.S., Paterson, M.S., 1969. The α - β Inversion in quartz: a coherent phase transition under nonhydrostatic stress. J. Geophys. Res. 74, 4921–4948. https://doi.org/10.1029/JB074i020p04921.

Dickinson, J.M., Armstrong, P.E., 1967. Temperature dependence of the elastic constants of molybdenum. J. Appl. Phys. 38, 602–606. https://doi.org/10.1063/1.1709381.

- Dolino, G., Bachheimer, J.P., Berge, B., Zeyen, C.M.E., 1984. Incommensurate phase of quartz: I. Elastic neutron scattering. J. Phys. 45, 361–371. https://doi.org/10.1051/ jphys:01984004502036100.
- Duffy, T.S., Ahrens, T.J., 1994. Dynamic response of molybdenum shock compressed at 1400 °C. J. Appl. Phys. 76, 835–842. https://doi.org/10.1063/1.357758.
- Gasc, J., Daigre, C., Moarefvand, A., Deldicque, D., Fauconnier, J., Gardonio, B., Madonna, C., Burnley, P., Schubnel, A., 2021. Deep focus earthquakes: from high temperature experiments to cold slabs. Geol. Submitted for publication.
- Getting, I.A., Christie, J.M., 1994. David tressel griggs. Natl. Acad. Press Biogr. Mem. 64. Ghaffari, H.O., Pec, M., 2020. An ultrasound probe array for a high-pressure, high-temperature solid medium deformation apparatus. Rev. Sci. Instrum. 91, 085117 https://doi.org/10.1063/5.0004035.
- Glover, P.W.J., Baud, P., Darot, M., Meredith, P.G., Boon, S.A., LeRavalec, M., Zoussi, S., Reuschlé, T., 1995. α/β phase transition in quartz monitored using acoustic emissions. Geophys. J. Int. 120, 775–782. https://doi.org/10.1111/j.1365-246X.1995.tb01852.x.
- Green, H.W., Borch, R.S., 1989. A new molten salt cell for precision stress measurement at high pressure. Eur. J. Mineral. 1, 213–220. https://doi.org/10.1127/ejm/1/2/
- Green, H.W., Scholz, C.H., Tingle, T.N., Young, T.E., Koczynski, T.A., 1992. Acoustic emissions produced by anticrack faulting during the olivine→spinel transformation. Geophys. Res. Lett. 19, 789–792. https://doi.org/10.1029/92GL00751.
- Gwanmesia, G.D., Rigden, S., Jackson, I., Liebermann, R.C., 1990. Pressure Dependence of Elastic Wave Velocity for beta-Mg2SiO4 and the Composition of the Earth's Mantle. Science 250, 794–797. https://doi.org/10.1126/science.250.4982.794.
- Hacker, B.R., Ritzwoller, M.H., Xie, J., 2014. Partially melted, mica-bearing crust in Central Tibet. Tectonics 33, 1408–1424. https://doi.org/10.1002/2014TC003545.
- Heilbronner, R., Stunitz, H., Précigout, J., Raimbourg, H., 2020. The solid medium deformation apparatus - reloaded (other). Oral. https://doi.org/10.5194/egusphereegu2020-9859.
- Hirth, G., Tullis, J., 1992. Dislocation creep regimes in quartz aggregates. J. Struct. Geol. 14, 145–159. https://doi.org/10.1016/0191-8141(92)90053-Y.
- Hirth, G., Tullis, J., 1994. The brittle-plastic transition in experimentally deformed quartz aggregates. J. Geophys. Res. Solid Earth 99, 11731–11747. https://doi.org/ 10.1029/93JB02873.
- Holyoke, C.W., Kronenberg, A.K., 2010. Accurate differential stress measurement using the molten salt cell and solid salt assemblies in the Griggs apparatus with applications to strength, piezometers and rheology. Tectonophysics 494, 17–31. https://doi.org/10.1016/j.tecto.2010.08.001.
- Incel, S., Hilairet, N., Labrousse, L., John, T., Deldicque, D., Ferrand, T., Wang, Y., Renner, J., Morales, L., Schubnel, A., 2017. Laboratory earthquakes triggered during eclogitization of lawsonite-bearing blueschist. Earth Planet. Sci. Lett. 459, 320–331. https://doi.org/10.1016/j.epsl.2016.11.047.
- Jacobsen, S.D., Spetzler, H.A., Reichmann, H.-J., Smyth, J.R., Mackwell, S.J., Angel, R.J., Bassett, W.A., 2002. Gigahertz ultrasonic interferometry at high *P* and *T*: new tools for obtaining a thermodynamic equation of state. J. Phys. Condens. Matter 14, 11525–11530. https://doi.org/10.1088/0953-8984/14/44/510.
- Ji, S., Wang, Q., 2011. Interfacial friction-induced pressure and implications for the formation and preservation of intergranular coesite in metamorphic rocks. J. Struct. Geol. 33, 107–113. https://doi.org/10.1016/j.jsg.2010.11.013.
- Johnson, S.E., Song, W.J., Cook, A.C., Vel, S.S., Gerbi, C.C., 2021. The quartz α↔β phase transition: does it drive damage and reaction in continental crust? Earth Planet. Sci. Lett. 553, 116622. https://doi.org/10.1016/j.epsl.2020.116622.
- Karato, S., Wenk, H.-R., Mineralogical Society of America, Geochemical Society (Eds.), 2002. Plastic Deformation of Minerals and Rocks, Reviews in Mineralogy & Geochemistry, Mineralogical Society of America, Washington, DC.
- Geochemistry. Mineralogical Society of America, Washington, DC.

 Kato, A., Iidaka, T., Ikuta, R., Yoshida, Y., Katsumata, K., Iwasaki, T., Sakai, S.,
 Thurber, C., Tsumura, N., Yamaoka, K., Watanabe, T., Kunitomo, T., Yamazaki, F.,
 Okubo, M., Suzuki, S., Hirata, N., 2010. Variations of fluid pressure within the
 subducting oceanic crust and slow earthquakes: fluid pressure variations and slow
 slips. Geophys. Res. Lett. 37 https://doi.org/10.1029/2010GL043723.
- Kern, H., 1982. Elastic-wave velocity in crustal and mantle rocks at high pressure and temperature: the role of the high-low quartz transition and of dehydration reactions. Phys. Earth Planet. Inter. 29, 12–23. https://doi.org/10.1016/0031-9201(82)90133-
- Kern, H., Richter, A., 1981. Temperature derivatives of compressional and shear wave velocities in crustal and mantle rocks at 6 Kbar confining pressure. J. Geophys. 49, 47, 56.
- Kido, M., Muto, J., Nagahama, H., 2016. Method for correction of differential stress calculations from experiments using the solid salt assembly in a Griggs-type deformation apparatus. Tectonophysics 672–673, 170–176. https://doi.org/ 10.1016/i.tecto.2016.02.011.
- Kind, R., Ni, J., Zhao, W., Wu, J., Yuan, X., Zhao, L., Sandvol, E., Reese, C., Nabelek, J., Hearn, T., 1996. Evidence from earthquake data for a partially molten crustal layer in Southern Tibet. Science 274, 1692–1694. https://doi.org/10.1126/ science.274.5933.1602
- Kirby, S.H., Kronenberg, A.K., 1984. Deformation of clinopyroxenite: evidence for a transition in flow mechanisms and semibrittle behavior. J. Geophys. Res. Solid Earth 89, 3177–3192. https://doi.org/10.1029/JB089iB05p03177.
- Kodaira, S., 2004. High Pore Fluid pressure May Cause Silent Slip in the Nankai Trough. Science 304, 1295–1298. https://doi.org/10.1126/science.1096535.
- Li, B., Liebermann, R.C., 2007. Indoor seismology by probing the Earth's interior by using sound velocity measurements at high pressures and temperatures. Proc. Natl. Acad. Sci. 104, 9145–9150. https://doi.org/10.1073/pnas.0608609104.

- Li, B., Jackson, I., Gasparik, T., Liebermann, R.C., 1996. Elastic wave velocity measurement in multi-anvil apparatus to 10 GPa using ultrasonic interferometry. Phys. Earth Planet. Inter. 98, 79–91. https://doi.org/10.1016/S0031-9201(96) 03173-1
- Lockner, D.A., Byerlee, J.D., Kuksenko, V., Ponomarev, A., Sidorin, A., 1991. Quasi-static fault growth and shear fracture energy in granite. Nature 350, 39–42. https://doi. org/10.1038/350039a0.
- McKnight, R.E.A., Moxon, T., Buckley, A., Taylor, P.A., Darling, T.W., Carpenter, M.A., 2008. Grain size dependence of elastic anomalies accompanying the α - β phase transition in polycrystalline quartz. J. Phys. Condens. Matter 20, 075229. https://doi.org/10.1088/0953-8984/20/7/075229.
- Meade, C., Jeanloz, R., 1989. Acoustic emissions and shear instabilities during phase transformations in Si and Ge at ultrahigh pressures. Nature 339, 616–618. https:// doi.org/10.1038/339616a0.
- Mechie, J., Sobolev, S.V., Ratschbacher, L., Babeyko, A.Y., Bock, G., Jones, A.G., Nelson, K.D., Solon, K.D., Brown, L.D., Zhao, W., 2004. Precise temperature estimation in the Tibetan crust from seismic detection of the α - β quartz transition. Geology 32, 601. https://doi.org/10.1130/G20367.1.
- Menegon, L., Nasipuri, P., Stünitz, H., Behrens, H., Ravna, E., 2011. Dry and strong quartz during deformation of the lower crust in the presence of melt. J. Geophys. Res. 116 https://doi.org/10.1029/2011JB008371.
- Mirwald, P.W., Massonne, H.-J., 1980. The low-high quartz and quartz-coesite transition to 40 kbar between 600° and 1600°C and some reconnaissance data on the effect of NaAlO 2 component on the low quartz-coesite transition. J. Geophys. Res. 85, 6983. https://doi.org/10.1029/JB085iB12p06983.
- Mirwald, P.W., Getting, I.C., Kennedy, G.C., 1975. Low-friction cell for piston-cylinder high-pressure apparatus. J. Geophys. Res. 80, 1519–1525. https://doi.org/10.1029/ JB080i011p01519.
- Mogi, K., 1962. Study of elastic shocks caused by the fracture of heterogeneous materials and its relations to earthquake phenomena. Bull. Earthq. Res. Inst. 東京大学地震研究所 40, 125–173.
- Nikitin, A.N., Markova, G.V., Balagurov, A.M., Vasin, R.N., Alekseeva, O.V., 2007. Investigation of the structure and properties of quartz in the α - β transition range by neutron diffraction and mechanical spectroscopy. Crystallogr. Rep. 52, 428–435. https://doi.org/10.1134/S1063774507030145.
- Okazaki, K., Hirth, G., 2016. Dehydration of lawsonite could directly trigger earthquakes in subducting oceanic crust. Nature 530, 81–84. https://doi.org/10.1038/nature16501.
- Paterson, M.S., 1970. A high-pressure, high-temperature apparatus for rock deformation. Int. J. Rock Mech. Min. Sci. Geomech. Abstr. 7, 517–526. https://doi.org/10.1016/ 0148-9062(70)90004-5.
- Paterson, M.S., Wong, T., 2005. Experimental Rock Deformation The Brittle Field. Springer Science & Business Media.
- Peacock, S.M., Christensen, N.I., Bostock, M.G., Audet, P., 2011. High pore pressures and porosity at 35 km depth in the Cascadia subduction zone. Geology 39, 471–474. https://doi.org/10.1130/G31649.1.
- Pec, Matej, Stünitz, Holger, Heilbronner, Renée, Druryc, Martyn, de Capitania, Christian, 2012. Origin of pseudotachylites in slow creep experiments. Earth and Planetary Science Letters 355–356, 299–310. https://doi.org/10.1016/j.epsl.2012.09.004.
- Peng, Z., Redfern, S.A.T., 2013. Mechanical properties of quartz at The α - β phase transition: Implications for tectonic and seismic anomalies: Quartz at the α - β phase transition. Geochem. Geophys. Geosyst. 14, 18–28. https://doi.org/10.1029/2012GC004482
- Pimienta, L., Schubnel, A., Violay, M., Fortin, J., Guéguen, Y., Lyon-Caen, H., 2018. Anomalous V p/V s ratios at seismic frequencies might evidence highly damaged rocks in subduction zones. Geophys. Res. Lett. 45, 12,210–12,217. https://doi.org/ 10.1029/2018GL080132.
- Popp, T., Kern, H., 1993. Thermal dehydration reactions characterised by combined measurements of electrical conductivity and elastic wave velocities. Earth Planet. Sci. Lett. 120, 43–57. https://doi.org/10.1016/0012-821X(93)90022-2.
- Précigout, J., Stünitz, H., Pinquier, Y., Champallier, R., Schubnel, A., 2018. High-pressure, high-temperature deformation experiment using the new generation Griggs-type apparatus. J. Vis. Exp. https://doi.org/10.3791/56841.

- Richter, B., Stünitz, H., Heilbronner, R., 2016. Stresses and pressures at the quartz-to-coesite phase transformation in shear deformation experiments. J. Geophys. Res. Solid Earth 121, 8015–8033. https://doi.org/10.1002/2016JB013084.
- Ringwood, A.E., Green, D.H., 1966. An experimental investigation of the Gabbro-Eclogite transformation and some geophysical implications. Tectonophysics 3, 383–427. https://doi.org/10.1016/0040-1951(66)90009-6.
- Rosenberg, C.L., Handy, M.R., 2005. Experimental deformation of partially melted granite revisited: implications for the continental crust. J. Metamorph. Geol. 23, 19–28. https://doi.org/10.1111/j.1525-1314.2005.00555.x.
- Rybacki, E., Renner, J., Konrad, K., Harbott, W., Rummel, F., Stöckhert, B., 1998.
 A Servohydraulically-controlled deformation apparatus for rock deformation under conditions of ultra-high pressure metamorphism. Pure Appl. Geophys. 152, 579–606. https://doi.org/10.1007/s000240050168.
- Schilling, F.R., Trumbull, R.B., Brasse, H., Haberland, C., Asch, G., Bruhn, D., Mai, K., Haak, V., Giese, P., Muñoz, M., Ramelow, J., Rietbrock, A., Ricaldi, E., Vietor, T., 2006. Partial melting in the central andean crust: a review of geophysical, petrophysical, and petrologic evidence. In: Oncken, O., Chong, G., Franz, G., Giese, P., Götze, H.-J., Ramos, V.A., Strecker, M.R., Wigger, P. (Eds.), The Andes. Springer, Berlin Heidelberg, pp. 459–474. https://doi.org/10.1007/978-3-540-48684-8 22.
- Scholz, C.H., 1968. Microfracturing and the inelastic deformation of rock in compression. J. Geophys. Res. 73, 1417–1432. https://doi.org/10.1029/JB073i004p01417.
- Shapiro, N.M., 2004. Thinning and flow of tibetan crust constrained by seismic anisotropy. Science 305, 233–236. https://doi.org/10.1126/science.1098276.
- Sheehan, A.F., de la Torre, T.L., Monsalve, G., Abers, G.A., Hacker, B.R., 2014. Physical state of Himalayan crust and uppermost mantle: Constraints from seismic attenuation and velocity tomography: Himalayan seismic attenuation. J. Geophys. Res. Solid Earth 119, 567–580. https://doi.org/10.1002/2013JB010601.
- Shen, A.H., Bassett, W.A., Chou, I.M., 1993. The α - β quartz transition at high temperatures and pressures in a diamond-anvil cell by laser interferometry. Am. Mineral. 78, 694–698.
- Shimada, M., Matsushita, K., Kuratani, S., Okamoto, T., Koizumi, M., Tsukuma, K., Tsukidate, T., 1984. Temperature dependence of young's modulus and internal friction in alumina, silicon nitride, and partially stabilized zirconia ceramics. J. Am. Ceram. Soc. 67, C–23-C-24. https://doi.org/10.1111/j.1151-2916.1984.tb09612.x.
- Takei, Y., 2017. Effects of Partial Melting on Seismic Velocity and Attenuation: a New Insight from experiments. Annu. Rev. Earth Planet. Sci. 45, 447–470. https://doi. org/10.1146/annurev-earth-063016-015820.
- Traylor, T., Burnley, P., Whitaker, M.L., 2019. Steady state deformation and ultrasonics: a study on the elasticity of polycrystalline Olivine. In: Abstr. MR31B-0081 Fall Meet. AGU San Franc.
- Tullis, J.A., 1979. High temperature deformation of rocks and minerals. Rev. Geophys. 17, 1137. https://doi.org/10.1029/RG017i006p01137.
- Tullis, T.E., Tullis, J., 1986. Experimental rock deformation techniques. Miner. Rock Deform. Lab. Stud. Am. Geophys. Union Wash. DC 36, 297–324.
- Vásárhelyi, B., 2010. Tribute to the first triaxial test performed in 1910. Acta Geod. Geophys. Hung. 45, 227–230. https://doi.org/10.1556/AGeod.45.2010.2.7.
- Wang, X.-Q., Schubnel, A., Fortin, J., David, E.C., Guéguen, Y., Ge, H.-K., 2012. High Vp/ Vs ratio: saturated cracks or anisotropy effects?: high vp/vs ratio-crack anisotropy? Geophys. Res. Lett. 39 https://doi.org/10.1029/2012GL051742.
- Wang, Y., Durham, W.B., Getting, I.C., Weidner, D.J., 2003. The deformation-DIA: a new apparatus for high temperature triaxial deformation to pressures up to 15 GPa. Rev. Sci. Instrum. 74, 3002–3011. https://doi.org/10.1063/1.1570948.
- Weiss, J., Grasso, J.-R., 1997. Acoustic Emission in Single Crystals of Ice. J. Phys. Chem. B 101, 6113–6117. https://doi.org/10.1021/jp963157f.
- Westbrook, J.H., 1958. Temperature Dependence of Strength and Brittleness of some Quartz Structures. J. Am. Ceram. Soc. 41, 433–440. https://doi.org/10.1111/j.1151-2916.1958.th12891.x
- Wittlinger, G., Farra, V., Hetényi, G., Vergne, J., Nábělek, J., 2009. Seismic velocities in Southern Tibet lower crust: a receiver function approach for eclogite detection. Geophys. J. Int. 177, 1037–1049. https://doi.org/10.1111/j.1365-246X.2008.04084 x.
- Zappone, A.S., Benson, P.M., 2013. Effect of phase transitions on seismic properties of metapelites: a new high-temperature laboratory calibration. Geology 41, 463–466. https://doi.org/10.1130/G33713.1.